The Astrophysical Journal Letters, 1006:L13 (26pp), 2026 July 20 https://doi.org/10.3847/2041-8213/ae84ba
© 2026. The Author(s). Published by the American Astronomical Society.
OPEN ACCESS

EP260321a/SN 2026gzf: The Faintest Shock Breakout Associated with a Broad-lined Supernova

Brendan O'Connor[1,24], Xander J. Hall[1], Malte Busmann[2,3], Daniel Gruen[2,3], Alberto Floris[2,4,5,6], Tomás Cabrera[1], Ziyuan Zhu[2], Antonella Palmese[1], Dylan Green[7], John Banovetz[7], Julius Gassert[1,2], Christopher L. Fryer[8,9], Roberto Ricci[10,11], Eleonora Troja[10], Surya Shivaprasad[2,3], Gregory R. Zeimann[12], Ariel J. Amsellem[1], Stephen Bailey[7], Segev BenZvi[13], Simone Dichiara[14], Hendrik van Eerten[15], Jeremy Hare[16,17,18], Lei Hu[1], Christopher M. Irwin[19], Keerthi Kunnumkai[1], Konstantin Malanchev[1], Mitra Maleki[2], Michael J. Moss[20], Adam D. Myers[21], Dheeraj Pasham[9,22], Christoph Ries[2], Geoffrey Ryan[23], David Schlegel[7], Michael Schmidt[2], Silona Wilke[2], and Yu-Han Yang[10]

[1] McWilliams Center for Cosmology and Astrophysics, Department of Physics, Carnegie Mellon University, Pittsburgh, PA 15213, USA; boconno2@andrew.cmu.edu, xhall@cmu.edu
[2] University Observatory, Faculty of Physics, Ludwig-Maximilians-Universität München, Scheinerstr. 1, 81679, Munich, Germany
[3] Excellence Cluster ORIGINS, Boltzmannstr. 2, 85748 Garching, Germany
[4] Institute of Astrophysics, FORTH, N.Plastira 100, Vassilika Vouton, 70013 Heraklion, Greece
[5] Department of Physics, University of Crete, Voutes University Campus, 70013 Heraklion, Greece
[6] National Institute for Astrophysics (INAF), Astronomical Observatory of Padova, IT-35122 Padova, Italy
[7] Lawrence Berkeley National Laboratory, 1 Cyclotron Road, Berkeley, CA 94720, USA
[8] Center for Nonlinear Studies, Los Alamos National Laboratory, Los Alamos, NM 87545, USA
[9] Department of Physics, The George Washington University, Washington, DC 20052, USA
[10] Dipartimento di Fisica, Università di Tor Vergata, Via della Ricerca Scientifica, 1, 00133 Rome, Italy
[11] INAF-Istituto di Radioastronomia, Via Gobetti 101, I-40129 Bologna, Italy
[12] University of Texas, Hobby–Eberly Telescope, McDonald Observatory, TX 79734, USA
[13] Department of Physics & Astronomy, University of Rochester, 206 Bausch and Lomb Hall, P.O. Box 270171, Rochester, NY 14627-0171, USA
[14] Department of Astronomy and Astrophysics, The Pennsylvania State University, 525 Davey Lab, University Park, PA 16802, USA
[15] Department of Physics, University of Bath, Building 3 West, Bath BA2 7AY, UK
[16] Astrophysics Science Division, NASA Goddard Space Flight Center, 8800 Greenbelt Road, Greenbelt, MD 20771, USA
[17] Center for Research and Exploration in Space Science and Technology, NASA/GSFC, Greenbelt, MD 20771, USA
[18] The Catholic University of America, 620 Michigan Avenue N.E., Washington, DC 20064, USA
[19] Astronomical Institute, Tohoku University, Sendai, Miyagi 980-8578, Japan
[20] NASA Postdoctoral Program Fellow, NASA Goddard Space Flight Center, Greenbelt, MD 20771, USA
[21] Department of Physics & Astronomy, University of Wyoming, 1000 E. University, Dept. 3905, Laramie, WY 82071, USA
[22] Eureka Scientific, 2452 Delmer Street, Suite 100, Oakland, CA 94602-3017, USA
[23] Perimeter Institute for Theoretical Physics, Waterloo, Ontario N2L 2Y5, Canada
Received 2026 June 3; revised 2026 June 24; accepted 2026 June 26; published 2026 July 14

Abstract

The explosion of a star is first marked by the shock wave breaking out of the stellar surface, producing a burst of ultraviolet and X-ray radiation. These events are observationally rare, despite likely accompanying the majority of supernovae (SNe). Here, we report on our multiwavelength observing campaign of the closest Einstein Probe fast X-ray transient (FXT) EP260321a at $z = 0.0344$. The thermal ($kT = 130$ eV) X-ray emission with peak luminosity of 1.0×10^{45} erg s^{-1} points to a shock breakout origin. We demonstrate that EP260321a is accompanied by a broad-lined Type Ic supernova, SN 2026gzf. The supernova (SN) properties, including its spectral evolution, lightcurve evolution, and expansion velocities, are all typical of the energetic stripped-envelope SNe associated with gamma-ray bursts (GRBs). However, deep X-ray upper limits obtained with the Chandra X-ray Observatory do not detect an X-ray afterglow, and instead exclude the afterglow of known GRBs or FXTs. If the stellar explosion launched a successful relativistic jet, we require that it had both a low Lorentz factor of $\Gamma_0 < 30$ and a kinetic energy of $E_{\rm kin} < 10^{49}$ erg for a stellar wind density of $A_* \gtrsim 1$. We propose that EP260321a originated from a mildly relativistic, weak outflow that was choked by the progenitor star. This scenario is capable of naturally explaining its low X-ray luminosity and lack of prompt gamma-ray emission. EP260321a bridges the gap between SN 2008D and low-luminosity GRBs, suggesting a greater diversity in the physical parameters of stripped stars as they undergo terminal collapse.

Unified Astronomy Thesaurus concepts: Time domain astronomy (2109); X-ray transient sources (1852); Core-collapse supernovae (304); Type Ic supernovae (1730)

Materials only available in the online version of record: machine-readable tables

1. Introduction

Supernova (SN) shock breakout marks the first electromagnetic signal produced when the explosion reaches the surface of the progenitor star or its surrounding circumstellar material. This brief flash encodes the radius, density structure,

[24] McWilliams Fellow.

Original content from this work may be used under the terms of the Creative Commons Attribution 4.0 licence. Any further distribution of this work must maintain attribution to the author(s) and the title of the work, journal citation and DOI.

and immediate environment (e.g., mass loss) of the star at the moment of core collapse, and therefore, provides the most direct probe of the final stage of massive star evolution (S. A. Colgate 1974; T. A. Weaver 1976; S. W. Falk 1978; R. I. Klein & R. A. Chevalier 1978; E. Nakar & R. Sari 2010, 2012; A. L. Piro et al. 2010; N. Sapir et al. 2011; B. Katz et al. 2012a, 2012b; G. Svirski & E. Nakar 2014a, 2014b; E. Waxman & B. Katz 2017; T. Faran & R. Sari 2019; C. L. Fryer et al. 2020, 2026; A. Levinson & E. Nakar 2020; C. M. Irwin et al. 2021; J. A. Goldberg et al. 2022; C. M. Irwin & K. Hotokezaka 2025a, 2025b). Although shock breakout is a generic prediction of SN theory, such that all supernovae (SNe) should exhibit breakout emission, direct detections are rare because the emission is short-lived and peaks in the extreme ultraviolet or soft X-ray band (S. Campana et al. 2006a; S. Gezari et al. 2008; K. Schawinski et al. 2008; A. M. Soderberg et al. 2008). The X-ray transient XRF 080109 associated with SN 2008D remains the clearest example of shock breakout to date (R. A. Chevalier & C. Fransson 2008; P. A. Mazzali et al. 2008; A. M. Soderberg et al. 2008; D. Malesani et al. 2009; M. Modjaz et al. 2009). Similar physics has also been invoked to explain the thermal high-energy components of nearby low-luminosity gamma-ray bursts (GRBs), including GRB 060218/SN 2006aj, GRB 100316D/SN 2010bh, and GRB 171205A/SN 2017iuk (S. Campana et al. 2006a; A. M. Soderberg et al. 2006; L.-X. Li 2007; X.-Y. Wang et al. 2007; E. Waxman et al. 2007; E. Nakar & R. Sari 2012; E. Nakar 2015; C. M. Irwin & R. A. Chevalier 2016; V. D'Elia et al. 2018; L. Izzo et al. 2019; C. M. Irwin & K. Hotokezaka 2025b). These events strongly suggest that shock breakout emission spans a continuum between ordinary SNe and relativistic explosions, depending on the progenitor's radius (e.g., E. Waxman & B. Katz 2017), circumstellar environmen and late-stage mass loss (e.g., D. Kasen 2010; A. J. Bayless et al. 2015; E. Lovegrove et al. 2017; N. Smith 2017; J. A. Goldberg et al. 2022; A. E. Niblett et al. 2025), outflow collimation (e.g., E. Nakar 2015; C. M. Irwin & R. A. Chevalier 2016), Lorentz factor (e.g., C. L. Fryer et al. 2026), and degree to which the jet successfully breaks out (or fails to break out) of the star (e.g., E. Nakar 2015; C. L. Fryer et al. 2026).

The soft X-ray band provides an optimal discovery channel to identify shock breakout emission from stripped-envelope SNe (e.g., D. Alp & J. Larsson 2020; A. J. Bayless et al. 2022; C. L. Fryer et al. 2026). These sources naturally display themselves as fast X-ray transients (FXTs). For example, SN 2008D was first serendipitously identified as an X-ray transient by the Swift X-ray Telescope (D. N. Burrows et al. 2005) before its SN nature was recognized (P. A. Mazzali et al. 2008; A. M. Soderberg et al. 2008), demonstrating that untargeted X-ray monitoring can reveal core-collapse explosions at phases inaccessible to optical surveys (see, e.g., A. J. Bayless et al. 2022). The launch of the Einstein Probe (EP; W. Yuan et al. 2015, 2022, 2025) has expanded this discovery space on a much larger scale. Instead of relying on serendipitous discovery with narrow field-of-view X-ray instruments (e.g., the Neil Gehrels Swift Observatory, N. Gehrels et al. 2004; A. M. Soderberg et al. 2008; the Chandra X-ray Observatory (CXO), P. G. Jonker et al. 2013; A. Glennie et al. 2015; F. E. Bauer et al. 2017; D. Alp & J. Larsson 2020; J. Quirola-Vásquez et al. 2022, 2023), the 3600 deg^2 view of EP has produced a rapid increase in the rate of FXT discoveries (B. O'Connor et al. 2025a; W. Yuan et al. 2025). Nearby EP transients associated with broad-lined Type Ic supernovae (SNe Ic-BL) offer a particularly important opportunity to probe the diversity of stellar death, the continuum of shock breakout emission from stripped stars, and their link to the collapsar progenitors of long-duration GRBs (see, e.g., S. E. Woosley 1993; A. I. MacFadyen & S. E. Woosley 1999; S. E. Woosley & J. S. Bloom 2006; J. Hjorth & J. S. Bloom 2012; Z. Cano et al. 2017a).

Several EP events have already been interpreted as shock breakout candidates (e.g., H. Sun et al. 2025; H. Hamidani et al. 2025; W. X. Li et al. 2025; R.-D. Liang et al. 2026). In particular, EP250108a and EP250827b have been proposed as relativistic shock breakouts associated with nearby SNe Ic-BL (R. A. J. Eyles-Ferris et al. 2025; W. X. Li et al. 2025; J. C. Rastinejad et al. 2025; G. P. Srinivasaragavan et al. 2025a, 2025b). These detections suggest that EP is finally revealing the predicted population of soft high-energy transients produced by shock breakout, mildly relativistic outflows, failed jets or cocoons, or dirty fireballs with lower bulk Lorentz factors than classical GRBs (e.g., J. E. Rhoads 2003). Therefore, EP is not only improving the census of FXTs in general, but also providing the first sizeable sample of events at the boundary between ordinary stripped-envelope SNe (e.g., A. Clocchiatti et al. 1996; A. V. Filippenko 1997; S. J. Prentice & P. A. Mazzali 2017), low-luminosity GRBs (e.g., S. Campana et al. 2006a; A. M. Soderberg et al. 2006), and jet-driven explosions (e.g., C. L. Fryer et al. 2025).

EP260321a is a recent FXT detected by the EP on 2026 March 21 (Q. J. Huang et al. 2026; W. Yuan et al. 2026). Initial reports of optical follow-up failed to identify a counterpart, with the exception of an archival source with blue color that displayed historical variability (T.-W. Chen et al. 2026; M.-H. Lee et al. 2026). Optical spectroscopy carried out with the Very Large Telescope showed that the archival point source was not a star, but instead colocated at a consistent redshift of $z = 0.0344$ with the coincident galaxy (N. R. Tanvir et al. 2026). Notably, this redshift is comparable to the distance of the low-luminosity GRBs 060218 ($z = 0.0331$; S. Campana et al. 2006b; E. Pian et al. 2006; A. M. Soderberg et al. 2006) and 171205A ($z = 0.0368$; V. D'Elia et al. 2018; L. Izzo et al. 2019), which are among the most nearby GRBs.

At this redshift ($z = 0.0344$), EP260321a displayed a peak X-ray luminosity of $L_X = (1.0 \pm 0.3) \times 10^{45}$ erg s^{-1}, which combined with its soft, thermal spectrum with $kT = 132^{+30}_{-21}$ eV, pointed to an SN shock breakout origin (Q. J. Huang et al. 2026; W. Yuan et al. 2026). In this scenario, the archival optical variability of the source can be explained by stellar outbursts as it approached its death (T.-W. Chen et al. 2026; N. R. Tanvir et al. 2026). Additional photometric and spectroscopic follow-up revealed the clear presence of excess emission at <1 day (T.-W. Chen et al. 2026; X. Liu et al. 2026; A. Martin-Carrillo et al. 2026), possibly attributed to the combination of shock cooling and circumstellar interaction (T.-W. Chen et al. 2026; A. Martin-Carrillo et al. 2026; W. Yuan et al. 2026). This was followed by a clearly rising SN lightcurve (A. de Ugarte Postigo et al. 2026; K. A. Sankar et al. 2026) and the onset of SN features in the optical spectra (G. Corcoran et al. 2026; J. Rastinejad et al. 2026; D. Xu et al.

2026), solidifying the shock breakout interpretation (W. Yuan et al. 2026).

Here, we present optical, near-infrared (NIR), and X-ray follow-up observations of EP260321a/SN 2026gzf over the first 60 days. We present a high-cadence multiwavelength lightcurve spanning the $ugrizJK_s$ filters starting less than 10 hr after discovery and a series of 12 optical spectra starting 3 days after discovery. We compare the lightcurves and spectra to other SNe Ic-BL and derive the properties of the SN ejecta. We further present X-ray and radio observations obtained with the CXO and Very Large Array (VLA) that constrain the presence of a relativistic outflow from EP260321a. For additional studies of EP260321a/SN 2026gzf that occurred both independently and simultaneously, see W. Yuan et al. (2026), J. C. Rastinejad et al. (2026), A. Martin-Carrillo et al. (2026), and T.-W. Chen et al. (2026).

Throughout the manuscript, we adopt a standard ΛCDM cosmology (Planck Collaboration et al. 2020) with $H_0 = 67.4$ km s^{-1} Mpc^{-1}, $\Omega_m = 0.315$, and $\Omega_\Lambda = 0.685$. At the transient's redshift of $z = 0.034328 \pm 0.000006$ (see Section 3.3), this corresponds to a luminosity distance of 158 Mpc. We adopt a rounded value of $z = 0.0344$ throughout the manuscript. All upper limits are reported at the 3σ level.

2. Observations

2.1. EP Discovery

EP260321a was first detected by the EP on 2026 March 21 at 12:30:18 UTC (Q. J. Huang et al. 2026; W. Yuan et al. 2026), which we hereafter adopt as T_0. The source was observed by the Wide-field X-ray Telescope (WXT) until $T_0 + 2200$ s and the Follow-up X-ray Telescope (FXT) from $T_0 + 1065$ to 2359 s (W. Yuan et al. 2026). The transient peaked at a 0.3–10 keV X-ray luminosity of $L_X = (1.0 \pm 0.3) \times 10^{45}$ erg s^{-1} at 690 s after the trigger (W. Yuan et al. 2026). The spectrum of the source was best fit with an absorbed blackbody with hydrogen column density $N_H = 8.4 \times 10^{20}$ cm^{-2} and a temperature ranging from $kT = 132^{+30}_{-21}$ eV measured over the first 500 s by WXT to $kT = 107.9^{+3.2}_{-3.0}$ over the last 500 s of the FXT observation (see Figure 1 and Table 2 of W. Yuan et al. 2026). The emission has been interpreted as SN shock breakout (Q. J. Huang et al. 2026; W. Yuan et al. 2026). We point the reader to W. Yuan et al. (2026) for further details on the observations and analysis of EP260321a. All values presented here are taken from W. Yuan et al. (2026).

2.2. Fraunhofer Telescope at Wendelstein Observatory

We observed the optical and NIR counterpart of EP260321a with the Three Channel Imager (3KK; F. Lang-Bardl et al. 2016) mounted on the 2.1 m Fraunhofer Telescope at Wendelstein Observatory (FTW; U. Hopp et al. 2014). Observations began on 2026 March 21 at 22:29:50 UT, corresponding to 0.41 day (9.84 hr) after the trigger. The 3KK camera is capable of obtaining images in three filters simultaneously: two optical and one near-infrared (NIR). We carried out daily observations in the *griz* bands as weather allowed. NIR observations (JK_s) were initially obtained simultaneously, but were not available after 2026 March 28 due to an issue with the cooling system. The cooling system was repaired, and NIR observations began again on 2026 April 22. The complete log of observations is tabulated in Table 1.

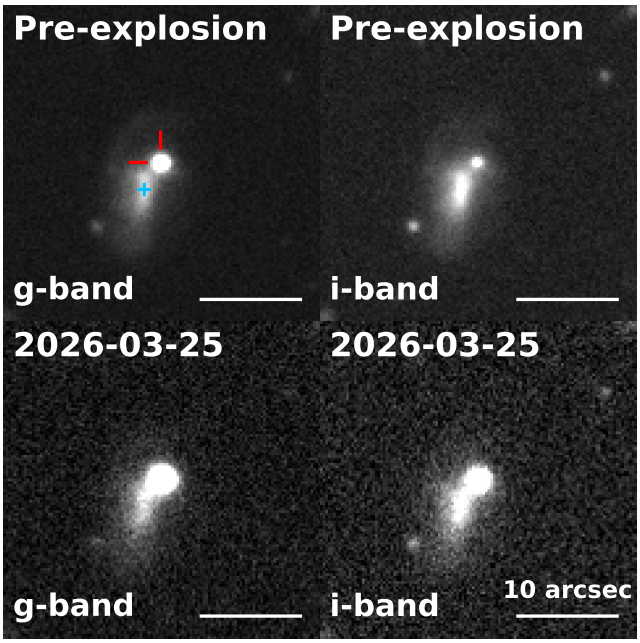

Figure 1. Finding chart of EP260321a/SN 2026gzf using DECam imaging in the *g* and *i* filters. Archival pre-explosion DECam images from 2013 (13 yr before discovery) are shown in the top panels, while the bottom panels show imaging obtained on 2026 March 25 ($T_0 + 3.6$ days). A blue point source ($g - i \approx -1.3$ mag) is visible at the location of the transient in archival imaging (see Appendix C). The transient explosion site (red crosshairs) is offset by 3.″4 from the center of the host galaxy (blue cross), corresponding to 2.5 kpc at $z = 0.0344$.

The FTW data were reduced using a custom pipeline (C. A. Gössl & A. Riffeser 2002) to perform bias and dark subtraction, flat-fielding, and cosmic-ray rejection. For more details, specifically with regard to the NIR data reduction, see M. Busmann et al. (2025). For optical images, we performed difference imaging with the Saccadic fast Fourier transform (`SFFT`) software[25] (L. Hu et al. 2022) using archival Pan-STARRS1 (PS1; K. C. Chambers et al. 2016), Sloan Digital Sky Survey (SDSS; e.g., K. N. Abazajian et al. 2009), and Legacy Survey (LS) images as templates. For the NIR imaging, we performed difference imaging with respect to the UKIRT Infrared Deep Sky Survey (A. Lawrence et al. 2007). We performed aperture photometry on the difference images using `Photutils` (L. Bradley et al. 2024) with AB magnitude zero-points calibrated to the PS1 (K. C. Chambers et al. 2016) and Two Micron All Sky Survey (M. F. Skrutskie et al. 2006) catalogs for optical and NIR data, respectively. The NIR photometry was converted from the Vega to the AB magnitude system using standard offsets. The photometry is reported in Table 1.

Despite the archival variability (T.-W. Chen et al. 2026) of the existing blue point source (Figure 19), we find that this variability is low level and does not have an impact on our lightcurve. We refer the reader to T.-W. Chen et al. (2026) for a more in-depth discussion of the source's variability and the link to SN 2026gzf. Here, we tested the possible impact of flux variations of the archival source in a few ways. First, we performed difference imaging versus multiple surveys (PS1, SDSS, and LS) using templates taken across multiple times, yielding negligible photometric deviations across all bands.

[25] https://github.com/thomasvrussell/sfft

Second, we performed an analysis of an archival time series and found no significant variability that would impact our photometry (see Figure 19 in Appendix C).

2.3. Dark Energy Camera

2.3.1. Targeted Follow-up

We observed EP260321a with the Dark Energy Camera (DECam) instrument mounted on the Blanco 4 m Telescope at the Cerro Tololo Inter-American Observatory using the *g*, *r*, and *z* bands (PI: Palmese; Table 1) starting on 2026 March 25, corresponding to 3.6 days after discovery. The images were astrometrically calibrated against Gaia DR3 (Gaia Collaboration 2020; Gaia Collaboration et al. 2021; L. Lindegren et al. 2021). We use `SFFT` (L. Hu et al. 2022) for image subtraction against archival DECam images and photometrically calibrate using PS1 (K. C. Chambers et al. 2016). See T. Cabrera et al. (2024), L. Hu et al. (2025, 2026) for further details on the DECam analysis pipeline. We show DECam imaging of the field as a finding chart in Figure 1.

2.3.2. Archival Image Analysis

We analyzed all archival *griz* images previously obtained by DECam. A blue compact source is detected at the location of the transient in all pre-explosion images, see Figure 1. These observations span the time range of 2013 June 21 to 2018 May 7, corresponding to 12.8–7.9 yr prior to the explosion. In total, there are 25, 17, 13, and 8 images in the *g*, *r*, *i*, and *z* bands, respectively. We performed point-spread function photometry of these images in each band to build archival lightcurves. This is displayed in Figure 19 in Appendix C, where we have further discussion of the origin of the pre-explosion source at the location of SN 2026gzf.

2.4. Dark Energy Spectroscopic Instrument

The Dark Energy Spectroscopic Instrument (DESI) includes 5000 independently positionable science fibers (E. F. Schlafly et al. 2023; C. Poppett et al. 2024). The spectrograph covers 3600–9824 Å at a spectral resolution of $R \sim 2000$–5500 (DESI Collaboration et al. 2016, 2025a, 2025b; T. N. Miller et al. 2024). The data were reduced and flux calibrated with the DESI spectroscopic data pipeline (J. Guy et al. 2023). DESI spectra are automatically corrected for Galactic extinction, which in this case is $E(B-V) = 0.02$ mag (E. F. Schlafly & D. P. Finkbeiner 2011).

DESI observed EP260321a on 2026 April 8, 2026 April 23, and 2026 May 14 (see Table 3) as part of a spare fiber program to observe Rubin transients (X. J. Hall et al. 2026a). For other examples of DESI spare fiber targets and observing strategy, see A. D. Myers et al. (2023), DESI Collaboration et al. (2024), and X. J. Hall et al. (2025, 2026c). The DESI spectra are publicly available through the DESI Transients Survey Zenodo (X. J. Hall et al. 2026b) as well as the Transient Name Server[26] and the Weizmann Interactive Supernova Data Repository (WISeREP; O. Yaron & A. Gal-Yam 2012).

2.5. Southern African Large Telescope

We obtained a spectroscopic sequence of EP260321a with the 10 m class Southern African Large Telescope (SALT; D. A. H. Buckley et al. 2006) starting on 2026 March 24. In total, we obtained eight spectra between the end of March and the end of 2026 May (Table 3). The initial spectrum was obtained through program 2025-2-SCI-016 (PI: X. Hall). Subsequent observations were acquired through a series of SALT Director's Discretionary Time proposals (2025-2-DDT-004, PI: B. O'Connor; 2026-1-DDT-003, PI: B. O'Connor). These additional spectra were obtained on 2026 March 27, 2026 April 1, 2026 April 5, and 2026 April 13 using the pg0700 grating at a camera station of 22.75 deg covering between 3592 and 7479 Å with a resolution of 735 at the central wavelength of 5580 Å and on 2026 May 2, 2026 May 9, and 2026 May 14 using the pg0700 grating at a camera station of 29.5 deg covering between 5250 and 9043 Å with a resolution of 953 at the central wavelength of 7202 Å. Each spectrum was obtained as a single exposure of 2100 s with 2×2 binning using a 1.″5 slit. The data were reduced using the RSS Long-slit spectra processing and extraction app `rsslsspectra`.[27] The complete log of spectral observations is tabulated in Table 3. The spectra are available through WISeREP.

2.6. Hobby–Eberly Telescope

We observed EP260321a with the 11 m Hobby–Eberly Telescope (HET; L. W. Ramsey et al. 1998; G. J. Hill et al. 2021) at McDonald Observatory under program M26-1-005 (PI: D. Gruen) on 2026 March 25. The observations were scheduled using the HET queue-scheduling system (M. Shetrone et al. 2007). We used the Low Resolution Spectrograph 2 (LRS2; T. S. Chonis et al. 2014, 2016) to obtain spectra in the blue channel LRS2-B. The raw LRS2 data were initially processed with `Panacea`,[28] which performs bias subtraction, dark subtraction, fiber tracing, fiber wavelength evaluation, fiber extraction, fiber-to-fiber normalization, source detection, source extraction, and flux calibration for each channel. The absolute flux calibration was performed using a spectrophotometric standard observed shortly after our observation. We extracted the flux-calibrated one-dimensional spectrum centered on the transient using the `LRS2Multi`[29] package. We present an analysis of the spatially resolved environment in Section 3.3.

2.7. Publicly Available Photometry

We queried publicly available photometry of EP260321a using the Babamul alert broker (T. Jegou du Laz et al. 2026). The object ID is 314003014107006318.[30] These include data obtained by the Zwicky Transient Facility (ZTF; E. C. Bellm et al. 2018; F. J. Masci et al. 2018; M. J. Graham et al. 2019) and the Vera C. Rubin Observatory (Ž. Ivezić et al. 2019). As EP260321a falls in the COSMOS Deep Drilling Field, the Rubin Legacy Survey of Space and Time (LSST) commissioning alerts are currently publicly available. While Rubin exhibits some possible pre-explosion detections, there are possible issues with the difference imaging at that stage (T. Ahumada et al. 2026). Therefore, we focus on Rubin data obtained after the discovery of EP260321a and do not include

[26] https://www.wis-tns.org/object/2026gzf

[27] https://astronomers.salt.ac.za/wp-content/uploads/sites/71/2024/09/rsslsspectra.pdf

[28] https://github.com/grzeimann/Panacea

[29] https://github.com/grzeimann/LRS2Multi

[30] https://babamul.caltech.edu/objects/LSST/314003014107006318

any pre-explosion Rubin photometry. ZTF data were obtained in the *gri* filters and Rubin data in the *ugriz* filters. A log of photometry from ZTF and Rubin is presented in Table 2.

2.8. CXO

We observed the position of EP260321a with CXO under program No. 27400339 (PI: B. O'Connor). Observations were carried out with ACIS-S starting on 2026 April 5 at 22:00 UT (T_0+15.4 days after the EP trigger) for a total of 19.81 ks. A second epoch was obtained starting on 2026 April 29 at 11:33:52 UT (T_0+39.0 days) for a total of 59.1 ks. The Chandra data were retrieved from the Chandra Data Archive (CDA).[31] We reprocessed the data using the `CIAO` v4.17.0 data reduction package with `CALDB v4.11.6`. The data were filtered to the 0.5–7 keV energy range. No source is detected at the location of EP260321a in either epoch, with a total of 0 photons within a 1.″5 radius at either phase. Adopting an annular background region with inner radius 30″ and outer radius of 60″, we find an expected number of 0.14 and 0.46 background counts within the 1.″5 radius circular source aperture in the first and second epochs, respectively. We adopt a typical GRB afterglow spectral shape with $p = 2.2$, which leads to a photon index of $\Gamma = 1.6$ for emission between the peak frequency and the cooling frequency (J. Granot & R. Sari 2002). This is a typical value identified by particle acceleration simulations (L. Sironi et al. 2015). We adopt a Galactic hydrogen column density of $N_{\rm H} = 2.5 \times 10^{20}$ cm^{-2} (R. Willingale et al. 2013). This absorbed power-law spectral shape yields 3σ upper limits of $<5.2 \times 10^{-15}$ and $<2.4 \times 10^{-15}$ erg cm^{-2} s^{-1}, respectively, on the 0.3–10 keV unabsorbed flux, which was derived using the `aplimits` tool available within `CIAO` (V. L. Kashyap et al. 2010). We note that these inferences are not particularly sensitive to the choice of photon index within the reasonably expected range for typical GRB afterglows. For a softer photon index $\Gamma = 3$, as observed for GRBs 060218 and 100316D (A. M. Soderberg et al. 2006; R. L. C. Starling et al. 2011; R. Margutti et al. 2013a), the derived 3σ limits are $<9.6 \times 10^{-15}$ and $<4.6 \times 10^{-15}$ erg cm^{-2} s^{-1}. This corresponds to an X-ray luminosity upper limit of roughly $<(1.3\text{–}2.9) \times 10^{40}$ erg s^{-1} at $z = 0.0344$.

2.9. VLA

The VLA observed EP260321a on 2026 May 19 at a mid-time of 23:15 UT (Program: SN 078192; PI: E. Troja), corresponding to 59.5 days after the EP trigger. The target was observed for 33 minutes (400 s on source) in A-array configuration using the C band at the center frequency of 6 GHz with a bandwidth of 4 GHz. The primary calibrator was 3C286, and the phase calibrator was J1024-0052. The data were flagged and calibrated in `CASA` v6.6.1 using the VLA continuum calibration pipeline (CASA Team et al. 2022). The calibrated dataset was imaged using the `CASA` task `tclean` with the weighting Briggs parameter set to 0.5 and 5000 `clean` iterations. No detection was found at the optical transient position down to a 3σ flux density upper limit of 42 μJy beam^{-1}.

3. Results

3.1. SN Lightcurve Analysis

3.1.1. Empirical Modeling

We performed an empirical fit to the lightcurves of SN 2026gzf in the *griz* bands following the approach outlined by F. Taddia et al. (2018, 2019) for modeling stripped-envelope SNe. The empirical model is given by

$$m(t) = \frac{y_0 + m(t - t_0) + g_0 \exp\left[-\frac{(t-t_0)^2}{2\sigma_0^2}\right]}{1 - \exp\left[\frac{\tau - t}{\theta}\right]}, \quad (1)$$

where y_0 and m describe the late-time linear decline, g_0, t_0, and σ_0 describe the Gaussian-like peak, and τ and θ control the exponential rise. The fit was performed using `emcee` (D. Foreman-Mackey et al. 2013) for each band individually. We used these fits to derive the peak time of the lightcurve t_p and the lightcurve decline rate parameter Δm_{15} in each band, where Δm_{15} is defined as the change in magnitude in a given filter over 15 days post-peak. The fit to each band is shown in Figure 2.

From this fit, for the *r* band, we derive $t_{p,r} = 15.0 \pm 0.5$ days and $\Delta m_{15,r} = 0.52^{+0.04}_{-0.02}$ mag; see also Figure 3. We compare this to other SNe Ic-BL in Figure 4, which is discussed further in Section 4.2. In the other bands we derive $t_{p,g} = 10.1 \pm 0.3$ days and $\Delta m_{15,g} = 1.19^{+0.03}_{-0.04}$ mag, $t_{p,i} = 15.5 \pm 0.6$ days and $\Delta m_{15,i} = 0.40^{+0.03}_{-0.04}$ mag, and $t_{p,z} = 18.3 \pm 0.7$ days and $\Delta m_{15,z} = 0.38^{+0.04}_{-0.05}$ mag.

In Figure 3, we compare the *r*-band lightcurve of SN 2026gzf to SNe Ic-BL associated with GRBs (hereafter GRB-SNe; J. Hjorth & J. S. Bloom 2012; Z. Cano et al. 2017a) and SNe Ic-BL associated with FXTs detected by the EP (hereafter FXT-SNe). We note that SN 2026gzf is itself an FXT-SN. Overall, the lightcurve shape of SN 2026gzf has good agreement with these SNe Ic-BL and with the SN Ib SN 2008D, despite SN 2008D being ∼2 mag fainter at peak (after correcting for intrinsic dust extinction; A. M. Soderberg et al. 2008); see Figure 4. We discuss this comparison to other SNe with high-energy associations further in Section 4.2.

3.1.2. Bolometric Lightcurve

We used simultaneous multiband imaging (Figure 2) obtained by FTW and DECam to build a bolometric lightcurve of SN 2026gzf. In general, DECam obtained data in the *griz* filters and FTW in the *grizJK*$_s$ filters, with the *u* band obtained at later phases by FTW and Rubin/LSST. By modeling the individual spectral energy distributions at each epoch with a blackbody, we can gauge the evolution of the total luminosity as well as the radius $R_{\rm BB}$ and temperature $T_{\rm BB}$. We note that the lack of pre-peak ultraviolet data can impact the temperature inferences at early times, which should be treated with caution.

We use the Hybrid Analytic Flux FittEr for Transients (`HAFFET`;[32] S. Yang & J. Sollerman 2023) to carry out this analysis. This method was previously used in A. Corsi et al. (2023), S. Anand et al. (2024), and G. P. Srinivasaragavan et al. (2024). The bolometric lightcurve, radius, and temperature are shown in Figure 5. The bolometric lightcurve is consistent, though at the luminous end, with inferences for other SNe Ic-BL both associated with GRBs and without any

[31] https://cda.harvard.edu/chaser/

[32] https://haffet.readthedocs.io/en/latest/

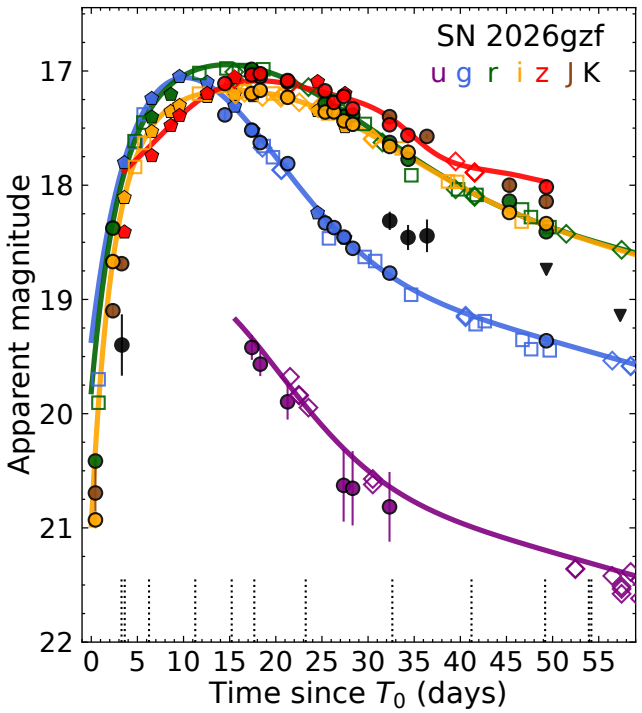

Figure 2. Multiband lightcurve (*ugrizJK*) of SN 2026gzf from FTW (filled circles), DECam (filled pentagons), ZTF (empty squares), and Rubin (empty diamonds). Solid lines are empirical fits using Equation (1) from F. Taddia et al. (2018). The vertical dashed lines at the bottom mark the timing of our spectroscopic observations.

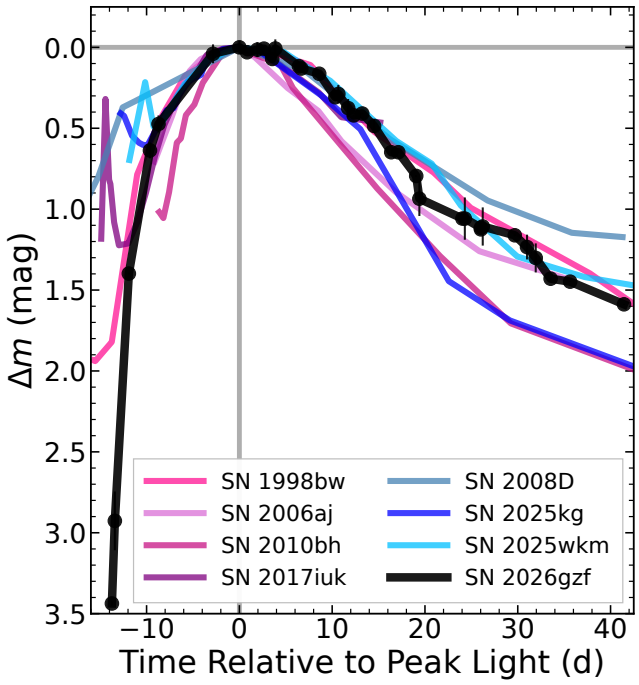

Figure 3. Lightcurve shape relative to peak brightness for SN 2026gzf (black) versus GRB-SNe (SNe 1998bw, 2006aj, 2010bh, and 2017iuk; T. J. Galama et al. 1998; S. Campana et al. 2006b; J. Sollerman et al. 2006; R. L. C. Starling et al. 2011; V. D'Elia et al. 2018; L. Izzo et al. 2019) and FXT-SNe (SNe 2008D, 2025 kg and 2025wkm; A. M. Soderberg et al. 2008; R. A. J. Eyles-Ferris et al. 2025; J. C. Rastinejad et al. 2025; G. P. Srinivasaragavan et al. 2025a, 2025b). The data are presented in either the *r* or *R* filters, and time has been converted to the rest frame.

GRB association (Z. Cano 2013; S. J. Prentice et al. 2016, 2019; F. Taddia et al. 2018; F. Taddia et al. 2019; G. P. Srinivasaragavan et al. 2024). The radii and temperature are also consistent with other SNe Ic-BL (e.g., F. Taddia et al. 2019; G. P. Srinivasaragavan et al. 2024). As observed by F. Taddia et al. (2019) and G. P. Srinivasaragavan et al. (2024), the radius increases until around 10 days after the maximum *r*-band light, which occurs ∼15 days after the EP trigger, and then begins to decrease as the photosphere begins to recede (L. Dessart et al. 2012). This behavior was also noted by A. Martin-Carrillo et al. (2026).

We likewise used `HAFFET` to carry out a semi-analytic Arnett (W. D. Arnett 1982) model fit to the bolometric lightcurve to derive the nickel mass $M_{\rm Ni}$ and diffusion timescale $\tau_{\rm m}$. We adopt a photospheric velocity of 20,000 km s^{-1} at maximum light. From the bolometric lightcurve in Figure 5, we infer a $M_{\rm Ni} = 0.45 \pm 0.02\,M_\odot$, $\tau_{\rm m} = 7.7^{+0.8}_{-0.5}$ days, total ejecta mass $M_{\rm ej} = 2.0^{+0.4}_{-0.3}\,M_\odot$, and kinetic energy $E_{\rm k} = (9.9^{+2.1}_{-1.3}) \times 10^{51}$ erg. These values are in good agreement with the average properties inferred from GRB-associated SNe Ic-BL by Z. Cano et al. (2017a), with typical values of $M_{\rm Ni} = 0.4 \pm 0.2\,M_\odot$ and $E_{\rm k} = (2.5 \pm 1.8) \times 10^{52}$ erg. Our inferred properties are consistent with the analyses of W. Yuan et al. (2026), T.-W. Chen et al. (2026), A. Martin-Carrillo et al. (2026), and J. C. Rastinejad et al. (2026), which broadly infer $M_{\rm Ni} \approx 0.3$–$0.5\,M_\odot$.

3.2. SN Spectral Analysis

3.2.1. Spectroscopic Evolution and Velocity Estimates

A series of optical spectra (Table 3) was obtained with SALT, HET, and DESI starting 3 days after discovery and extending to 55 days. The sequence of spectra is shown in Figure 6. The spectra show a clear evolution and display the broad absorption features expected in SNe Ic-BL. This is consistent with the initial classification of SN 2026gzf as an SN Ic-BL (G. Corcoran et al. 2026; J. Rastinejad et al. 2026; D. Xu et al. 2026). From nebular emission lines within the host galaxy (no absorption lines are detected), we derive a redshift of $z = 0.0343588 \pm 0.0000015$ using the HET Integral Field Unit (IFU) dataset (see Section 3.3). The redshift is consistent to the third decimal place across the entire host galaxy, including at the transient location. This is consistent with the redshift ($z = 0.034328 \pm 0.000006$) of the host galaxy[33] inferred from archival DESI spectra (Target ID: 39627799320858502[34]) available in Data Release 1[35] (DESI Collaboration et al. 2026). In what follows, we refer to measured wavelengths in the rest frame of SN 2026gzf.

Our first spectra (Figure 6) were obtained at ∼3 days, roughly ∼12 days before peak optical light (Figure 2). The early spectra show a blue slope with absorption features at ∼4600 Å and 5900 Å. We note that at early times (<10 days), the spectral shape of the SALT data is unreliable below 4200 Å, due to a lack of spectrophotometric standards. The HET data obtained at 3.6 days have a trustworthy spectral shape over the full range, as a spectrophotometric standard was observed nearly simultaneously, and we base our analysis of

[33] We note that the DESI fiber placement in this observation is offset from the center of the host galaxy and located in the "wings" of its light profile due to an issue with the LS source detection (Tractor catalog) that falsely identifies a source at that location.

[34] https://www.legacysurvey.org/viewer/desi-spectrum/dr1/targetid39627799320858502

[35] https://vizier.cds.unistra.fr/viz-bin/VizieR?-source=V/161

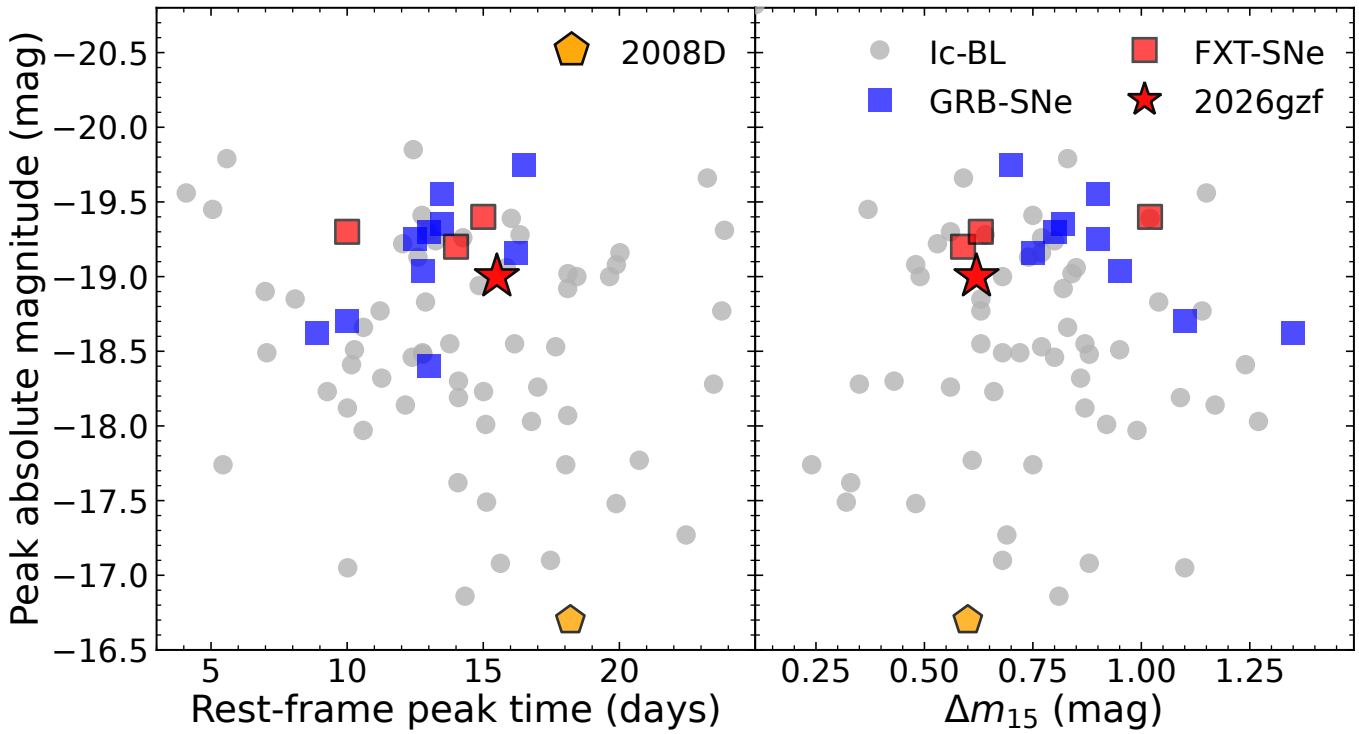

Figure 4. A comparison of EP260321a/SN 2026gzf to other SNe Ic-BL, both associated with GRBs and identified independently through optical surveys. The left panel shows the peak absolute magnitude vs. the rest-frame peak time, and the right panel shows the absolute magnitude vs. Δm_{15}, which represents the fade rate over 15 days relative to the peak time. GRB-SNe are shown using the *V* band, while other SNe Ic-BL, including SN 2026gzf, are shown using the *r* band. The data have been taken from (Z. Cano 2013; Z. Cano et al. 2014, 2017a; F. Taddia et al. 2018; G. P. Srinivasaragavan et al. 2024, 2025b; J. C. Rastinejad et al. 2025; L. Cotter et al. 2026).

the ∼3 day spectra on this. In general, this has no impact on our conclusions or inferences.

By 11.3 days, these early absorption features become clearer and evolve to be significantly deeper at ∼4700 and ∼6000 Å. While the 11.3 day spectrum is noisy due to being obtained in cloudy conditions, these features are clearly observed in all subsequent higher signal-to-noise spectra, supporting their existence at 11.3 days. We associate these features around 4700 and 6000 Å with a blueshifted Fe II$\lambda\lambda$4924, 5018, 5169 multiplet 42 (hereafter, Fe IIλ5169) and Si IIλ6355 absorption, respectively. We utilize these rest-frame wavelengths to derive the photospheric expansion velocity associated with these absorption features as a function of time following the methods outlined by G. Finneran et al. (2025a). For the Fe IIλ5169 feature, we infer a high velocity of ∼35,000 km s^{-1} at 3.6 days, decreasing to ∼20,000 km s^{-1} by 11.3 days and remaining relatively constant out to 55 days. We infer similarly high velocities by associating the absorption feature at ∼6000 Å with Si IIλ6355. We observe this feature to continuously decline with time from ∼29,000 km s^{-1} at 3.6 days to ∼10,000 km s^{-1} at 32.6 days. We show the velocity evolution in Figure 8.

In DESI spectra obtained at 17.7, 32.6, and 53.6 days (Figures 6 and 7), spanning from shortly after optical maximum to several weeks after peak, we see an additional absorption trough at ∼8000 Å. We interpret this as the Ca II triplet consisting of lines at 8498 Å, 8542 Å, and 8662 Å. Here, we adopt the *gf*-weighted centroid of 8579 Å. We note a mean wavelength of 8567 Å is also sometimes adopted in the literature, but this is less physically motivated than using the oscillator strength weighted value we adopt here. This Ca II feature shows a clear P Cygni profile, which becomes increasingly clear at later times; see the 53.6 day DESI spectrum in Figure 7.

As our earlier SALT spectra do not cover past 7200 Å we cannot probe the earlier velocity evolution of this feature, but we can constrain the velocity to be less than 45,000 km s^{-1} between 3.3 and 15.3 days. Based on the DESI spectra, we infer Ca II velocities of ∼20,000 km s^{-1} at 17.7 days. The velocity stays relatively constant out to 55 days (Figure 8). In some SNe Ic-BL, this feature can become blended with O Iλ7774 or Mg II$\lambda\lambda$7877, 7896 (*gf*-weighted value of λ7889). However, the observed feature lies redward of these lines and they are unlikely to contribute sufficiently. Instead, assuming the same blueshifted expansion velocity as inferred for Ca II, we find that O Iλ7774 and Mg II$\lambda\lambda$7877, 7896 may be producing a lower-significance broad absorption feature near 7200–7400 Å, as seen in the DESI spectra (Figure 6).

We also note that in our final DESI spectrum at 53.6 days, additional spectral features, possibly in emission, appear to be developing at ∼5900 and ∼7100 Å; see Figure 7. The latter feature has a broader visible rise in the continuum over ∼7100–7400 Å. The exact identification of these features is uncertain (see, e.g., P. A. Mazzali et al. 2001; K. Maeda et al. 2006), and additional spectra are required to confirm their significance and evolution.

3.2.2. Comparison to Other SNe Ic-BL Spectra and Velocities

In Figure 9, we compare the DESI spectra obtained at 17.7 days (near peak optical light) to other SNe Ic-BL. We find a good match to high-velocity GRB-SN such as GRB 060218/SN 2006aj (S. Campana et al. 2006a; P. Ferrero et al. 2006; P. A. Mazzali et al. 2006; E. Pian et al. 2006; A. M. Soderberg

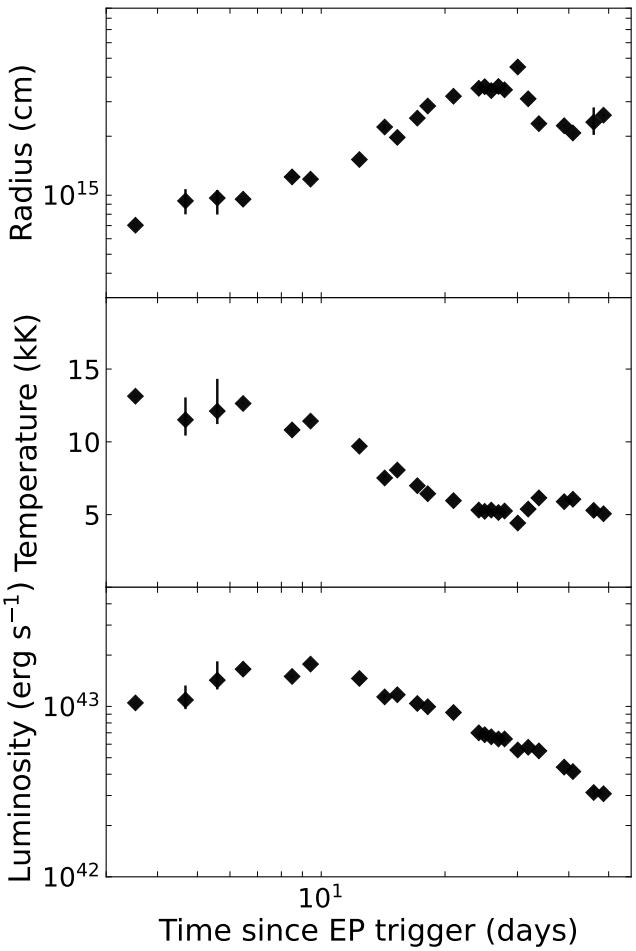

Figure 5. Evolution of the inferred photospheric radius, temperature, and bolometric luminosity of SN 2026gzf. Given the lack of UV data, the inferences at <1 day are less secure and are excluded.

et al. 2006; J. Sollerman et al. 2006), GRB 130702A/SN 2013dx (V. D'Elia et al. 2015; V. L. Toy et al. 2016; A. A. Volnova et al. 2017; P. A. Mazzali et al. 2021), and GRB 171205A/SN 2017iuk (V. D'Elia et al. 2018; J. Wang et al. 2018; L. Izzo et al. 2019) at similar phases. While the exact velocity of each SN differs, similar features clearly exist in each spectrum and provide a definitive classification of SN 2026gzf as an SN Ic-BL.

We next compare the inferred Fe II and Si II velocities and their evolution to a sample of GRB-SNe and non-GRB-associated SNe Ic-BL from G. Finneran et al. (2025a). In Figure 10, we show the velocity versus time for both features. There is good agreement between our inferences and other SNe Ic-BL of both classes. The initially high velocities (>30,000 km s^{-1}) for both features have better agreement with GRB-SNe, which tend to have higher velocities than non-GRB SNe Ic-BL (see M. Modjaz et al. 2016; G. Finneran et al. 2025a). While SN 2026gzf is not associated with a GRB and shows instead a soft thermal blackbody prompt emission spectrum (Q. J. Huang et al. 2026), the existence of high velocities and a luminous peak absolute magnitude (Figure 4) may indicate that a central engine helped drive more energy into the SN ejecta than in non-GRB/non-FXT associated, optically selected SNe Ic-BL. We discuss this further below.

From their compiled sample, G. Finneran et al. (2025a) derive median velocities of ∼21,000 km s^{-1} from Fe II and ∼17,000 km s^{-1} Si II at 15 days. This is in good agreement with our results for SN 2026gzf (Figure 10). It is not uncommon to infer larger velocities (by up to even $\Delta v \approx$ 10,000–20,000 km s^{-1}; see Figure 25 of G. Finneran et al. 2025a) from Fe II than from Si II, and the velocity evolution can have a different temporal dependence, as seen also for SN 2026gzf.

3.3. Spatially Resolved Analysis of the Environment

We extracted spectra from individual HET LRS2 spaxels at selected positions across the IFU field in order to investigate both the transient environment and the properties of the host galaxy. The data cube was resampled to a spaxel scale of $0\farcs4 \times 0\farcs4$, corresponding to a projected physical scale of approximately 280 × 280 pc at the redshift of the host. We note that the transient is located $\sim 3\farcs4$ from the center of the host galaxy (Figure 1), which corresponds to roughly 2.5 kpc.

We measured the redshift in multiple locations employing the brightest detected emission lines across the galaxy, in particular Hβ, Hα, and the [O III]$\lambda\lambda$4959, 5007 doublet, which are consistently detected across the IFU field. From these measurements, we obtain a weighted mean redshift of $z = 0.0343588 \pm 0.0000015$, with the weights determined from the signal-to-noise ratio (S/N) of each extracted spectrum. The measured redshift is consistent, within the uncertainties, across the full spatial extent of the galaxy.

Additionally, for each spaxel we measured the narrow emission-line fluxes by fitting the Hβ, [O III]λ5007, Hα, and [N II]λ6583 lines with Gaussian profiles. These fluxes were used to construct a [N II]-based Baldwin–Phillips–Terlevich (BPT) diagram (J. A. Baldwin et al. 1981) as described in Figure 11. Uncertainties on the measured fluxes were estimated from the continuum noise in the vicinity of each fitted line. The corresponding line ratio uncertainties were then propagated from the measured flux uncertainties in logarithmic space. To ensure a robust classification, we retained only spaxels for which all relevant diagnostic lines were securely detected, requiring a minimum S/N of at least 3.

The resulting spatially resolved [N II] BPT diagram shows that the vast majority of spaxels lie within the H II region locus. An [O I]-based BPT diagram provides a consistent conclusion. Figure 11 indicates that the ionization across the region surrounding the transient and the host galaxy is dominated by star formation. We further observe that the transient location differs from the rest of the host galaxy in terms of its location in the BPT diagram. The explosion site of EP260321a/SN 2026gzf has a substantially lower value of the ratio N2 ≡ log([N II]/Hα), suggesting a metallicity gradient from the explosion site to the galaxy center. In particular, at the SN location we measure log([O III]/Hβ) = 0.87 ± 0.01 and N2 = −1.84 ± 0.03, placing it in the upper left region of the H II region in Figure 11.

We additionally derive O3N2 ≡ log(([O III] 5007/Hβ)/([N II] 6583/Hα)) = 2.72 ± 0.03. We use the N2 and O3N2 ratios to derive the metallicity at the explosion site using the calibrations from M. Pettini & B. E. J. Pagel (2004) and R. A. Marino et al. (2013). This yields a consistently low metallicity inferred from the oxygen abundance 12 + log(O/H) ≈ 7.85–7.95. This corresponds to an extremely subsolar metallicity of 0.15–0.2 $Z_\odot$ (C. Allende Prieto et al. 2001; M. Asplund et al. 2004, 2009), and is more comparable to the SMC inferred values (S. C. Russell & M. A. Dopita 1990).

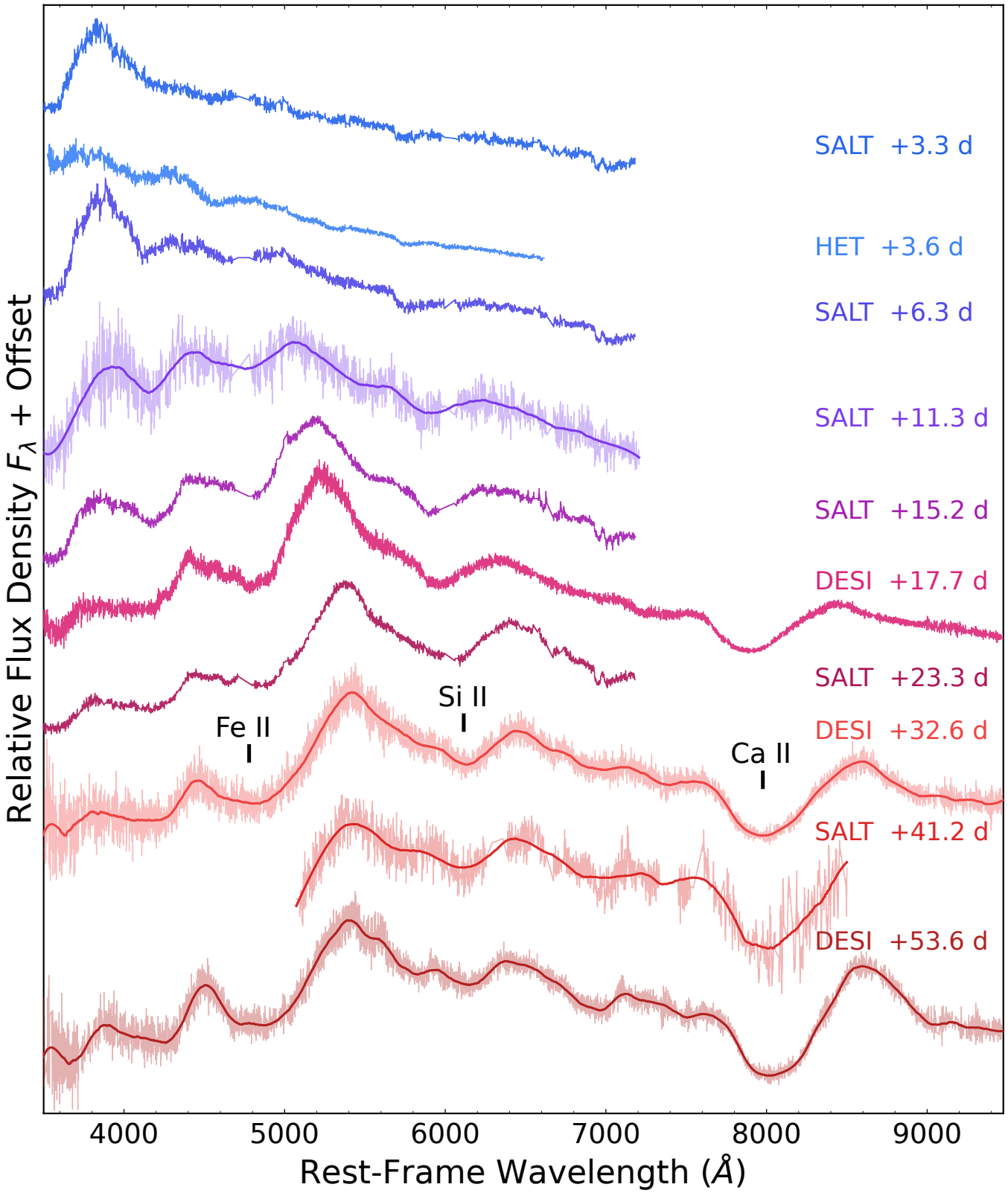

Figure 6. Spectral sequence of EP260321a/SN 2026gzf obtained with SALT, HET, and DESI between 3.3 and 53.6 days after the EP trigger. Blueshifted absorption features of Fe II, Si II, and Ca II that are used for our analysis in Sections 3.2.1 and 3.2.2 are marked for clarity. Emission lines have been clipped from the spectra for clarity. Some spectra are smoothed with a Savitzky–Golay filter (thick lines) for visualization purposes, and the unsmoothed spectra (thin lines) are also shown for completeness. The spectral shape of the SALT data obtained prior to 10 days is uncertain below 4200 Å.

We note that the statistical uncertainty (±0.02) on the oxygen abundance is significantly smaller than the systematic uncertainty (0.1–0.2 dex) on these calibrations (M. Pettini & B. E. J. Pagel 2004; R. A. Marino et al. 2013). We note our inferred values for O3N2 and N2 lie outside the range of values used to define these oxygen abundance calibrations, and should

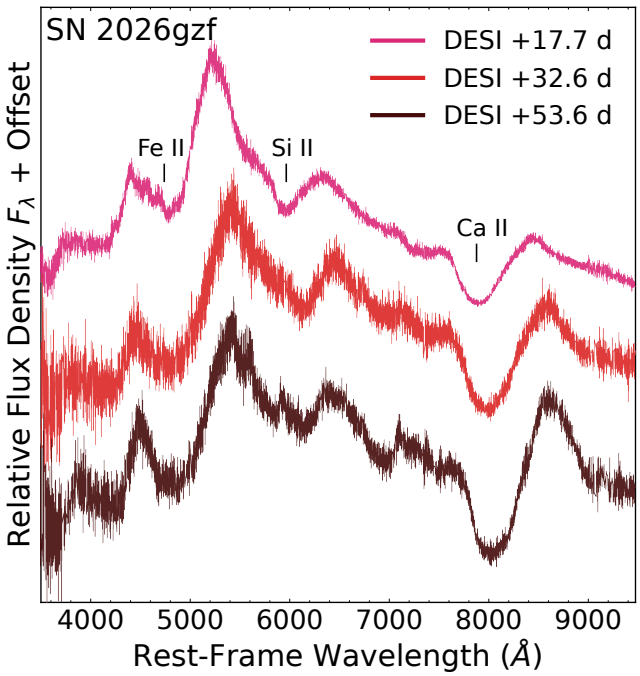

Figure 7. Evolution of the DESI spectra ($R \sim 2000$–5500) of SN 2026gzf obtained at 17.7, 32.6, and 53.6 days. Blueshifted absorption features of Fe II, Si II, and Ca II that are used for our analysis in Sections 3.2.1 and 3.2.2 are marked for clarity. Nebular emission lines have been clipped from each spectrum for visualization purposes. Spectra have not been smoothed and are in their native binning.

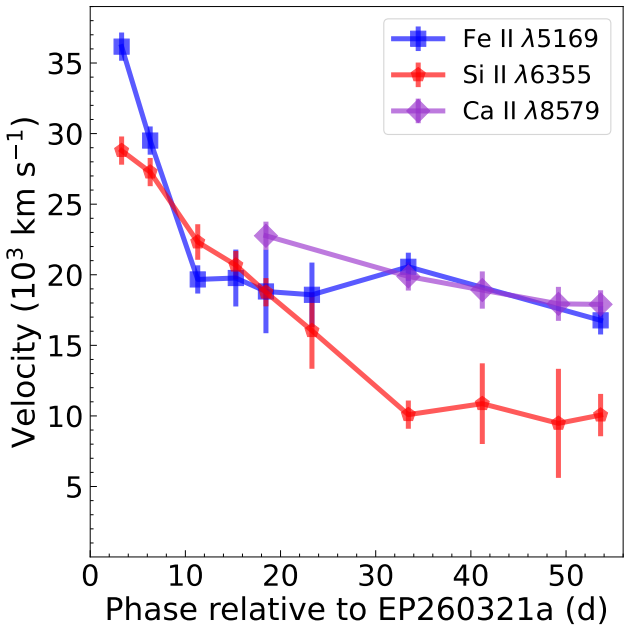

Figure 8. Evolution of the expansion velocity of different absorption features identified in the spectral sequence of SN 2026gzf (Figure 6).

be interpreted as generally indicative of an extremely low-metallicity environment. As we derive consistent values across multiple diagnostic ratios and multiple calibrations, we consider this a robust interpretation of the data.

While we observe a clear trend in the BPT diagram (Figure 11) of decreasing N2, and therefore decreasing metallicity, moving from the transient location to the rest of the host galaxy, the metallicity of the galaxy is still extremely

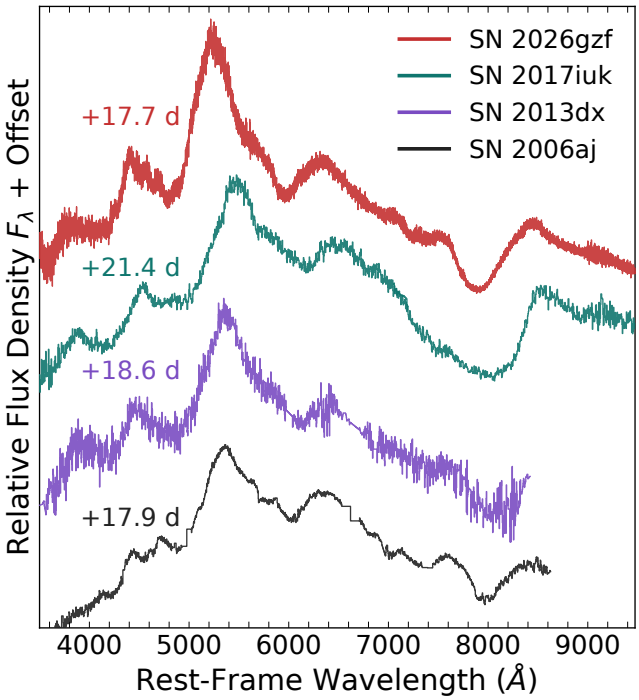

Figure 9. Comparison of the DESI spectra of SN 2026gzf obtained at 17.7 days after discovery vs. other SNe Ic-BL at a similar phase. Nebular emission lines have been clipped from each spectrum for visualization purposes. Spectra have not been smoothed and are in their native binning.

subsolar, lying at a similar location to other GRB explosion sites (L. Christensen et al. 2008; X. H. Han et al. 2010; E. M. Levesque et al. 2011, 2012; C. C. Thöne et al. 2014, 2024; L. Izzo et al. 2017). Using the spectra extracted from the spaxel covering the center of the host galaxy, we derive $N2 = -1.18 \pm 0.06$ and $O3N2 = 1.70 \pm 0.06$, yielding $12 + \log(O/H) = 8.20 \pm 0.04$, otherwise denoted as $0.3\,Z_\odot$ (M. Asplund et al. 2009). The derived value agrees between the different calibrations (M. Pettini & B. E. J. Pagel 2004; R. A. Marino et al. 2013).

Additionally, by extracting spectra from within a 3 spaxel radius of the center of the transient and host galaxy, we derive Hα inferred (R. C. J. Kennicutt 1998) star formation rates (SFRs) of 0.20 ± 0.01 and $0.07 \pm 0.01\,M_\odot$ yr^{-1} for the transient explosion site and host galaxy, respectively. In this analysis, we adopted a Chabrier (G. Chabrier 2003) initial mass function.

3.4. Afterglow Constraints

Here, we compute the allowed parameters for nondetection of a synchrotron afterglow (R. Sari et al. 1998; J. Granot & R. Sari 2002) using the `VegasAfterglow` package (Y. Wang et al. 2026). We model the afterglow with a Gaussian-structured jet propagating into a wind environment characterized by $\rho(r) \propto r^{-2}$. The physical setup is specified by eight parameters: the isotropic-equivalent kinetic energy at the jet's core $E_{\rm kin}$, the Lorentz factor at the jet's core Γ_0, the jet's core half-opening angle θ_c, the observer's viewing angle θ_v, the density A_*, the magnetic and electron energy fractions ε_B and ε_e, and the electron power-law index p.

Following B. O'Connor et al. (2025c), we generate afterglow models across a broad grid of parameters and compare the flux density at each time and frequency to our X-ray upper

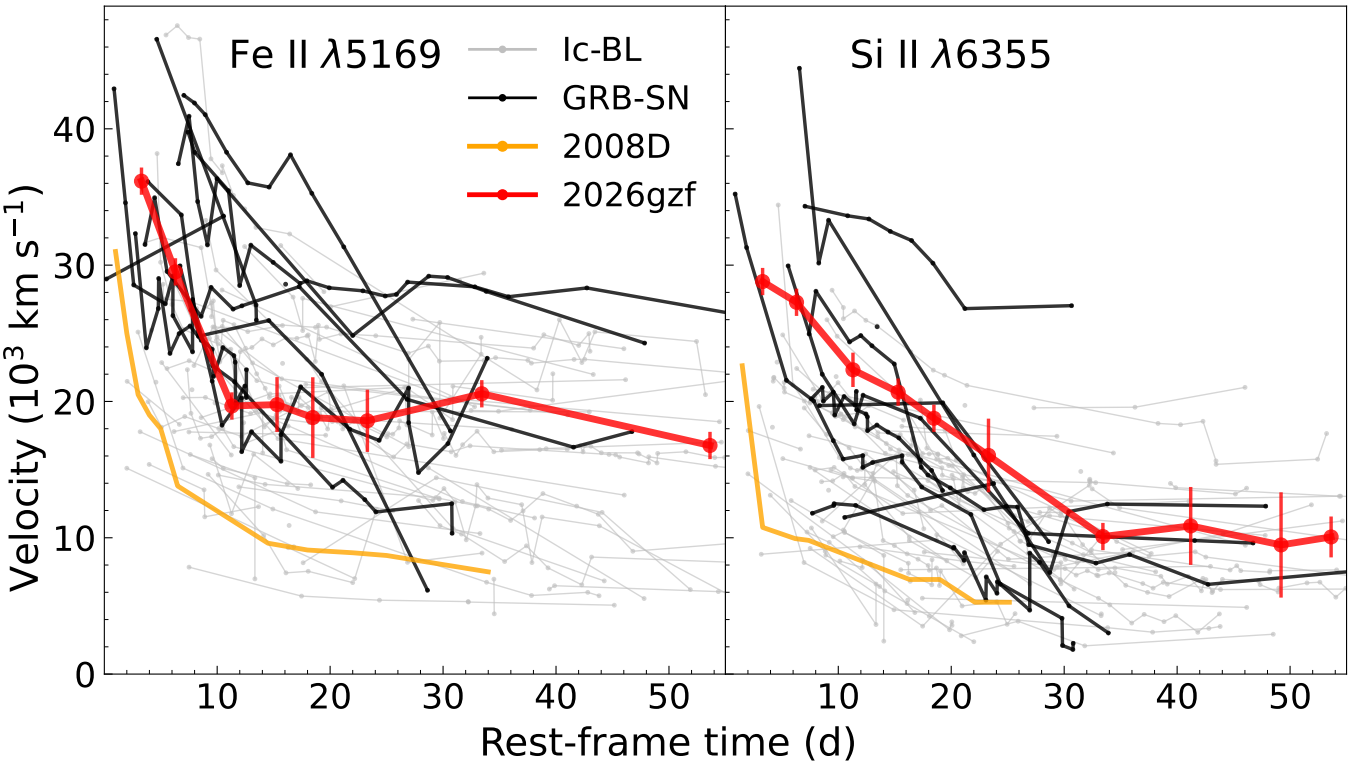

Figure 10. Velocity evolution of SNe Ic-BL (gray) and GRB-SN Ic-BL black) from G. Finneran et al. (2025a) to SN 2026gzf (red). The left panel shows the evolution of Fe IIλ5169, and the right panel shows Si IIλ6355. Velocities for SN 2008D are reproduced from P. A. Mazzali et al. (2008) and D. Malesani et al. (2009).

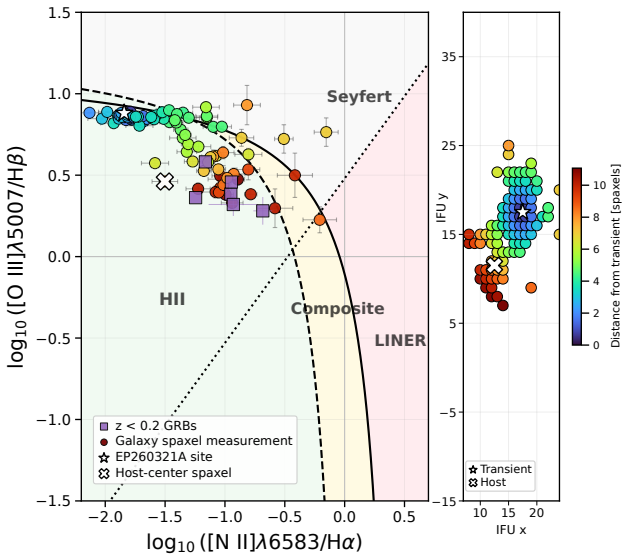

Figure 11. Spatially resolved [N II] BPT diagram from HET-IFU spectroscopy. Each point represents an individual galaxy spaxel, with emission-line ratios following the BPT diagnostics of J. A. Baldwin et al. (1981). Points are color-coded by projected distance from the transient position, as shown in the IFU field map on the right with units of the spaxel ($0\farcs4 \times 0\farcs4$) grid. The dashed, solid, and dotted curves indicate the G. Kauffmann et al. (2003) star-forming/composite boundary, the L. J. Kewley et al. (2001) maximum starburst boundary, and the L. J. Kewley et al. (2006) Seyfert/LINER division, respectively. The shaded regions show the corresponding H II-like region, composite, Seyfert, and LINER-like classifications. The transient site is marked by a white star, while the location of the galaxy center is shown with a white cross. GRB explosion site measurements at $z < 0.2$ are shown as purple squares (L. Christensen et al. 2008; X. H. Han et al. 2010; E. M. Levesque et al. 2011, 2012; C. C. Thöne et al. 2014, 2024; L. Izzo et al. 2017).

limits. We also include multifrequency radio upper limits from the VLA (This work, Section 2.9; and J. K. Leung et al. 2026) and require that the early X-ray afterglow is fainter than the initial EP detections (Q. J. Huang et al. 2026).

Over a dense scan spanning $p = 2.2$–2.8, $A_* = 10^{-4}$–10^{2}, $E_{\rm kin} = 10^{48}$–10^{52} erg, $\theta_c = 0.05$–0.25, $\theta_{\rm v}/\theta_{\rm c} = 0$–$6$, and $\epsilon_B = 10^{-4}$–10^{-1} with fixed $\Gamma_0 = 100$, only $\sim$1% of models remain allowed by the X-ray and radio upper limits. More specifically, wind models with $\theta_{\rm v}/\theta_{\rm c} \lesssim 3$ are almost entirely excluded, and even near $\theta_{\rm v}/\theta_{\rm c} \sim 3$, only a very small region at low A_* and low ϵ_B survives. We note that excluding the requirement that the X-ray afterglow is fainter than the initial EP detections increases the allowed models over this grid to 28%. However, the lack of an X-ray afterglow at early times and the lack of a power-law X-ray spectrum are confirmed by the early EP/FXT observations reported by W. Yuan et al. (2026).

The allowed region shrinks rapidly as either A_* or ϵ_B increases. For example, in the fixed slice with $\theta_{\rm c} = 0.15$ and $\epsilon_B = 10^{-2}$, the entire explored wind parameter space for $A_* = 0.1$–10 and $\theta_{\rm v}/\theta_{\rm c} = 0, 2, 4, 6$ is excluded. For densities below $A_* \lesssim 0.1$, the allowed parameter space rapidly expands (see Figure 12 and Figure 18 in Appendix B). However, given the pre-explosion activity of the transient (Appendix C; T.-W. Chen et al. 2026; W. Yuan et al. 2026), which is likely due to instabilities and eruptive mass loss, we find it unlikely that the surrounding environment is pristine, and instead expect a higher density.

As such, for fixed $A_* = 1$, $\theta_{\rm c} = 0.15$ rad, $\varepsilon_{\rm e} = 0.1$, $\varepsilon_{\rm B} = 0.01$, and $p = 2.2$, we compute the allowed Lorentz factor and isotropic-equivalent kinetic energy at the jet's core. The results

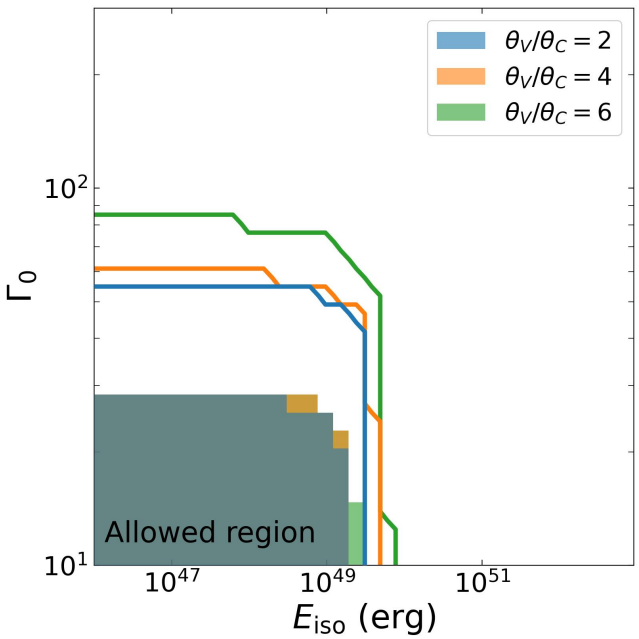

Figure 12. Allowed parameter space (shaded regions) of initial Lorentz factor Γ_0 at the jet's core and the jet's core kinetic energy $E_{\rm kin}$ for afterglow nondetection, assuming a Gaussian-structured jet at 158 Mpc ($z = 0.0344$) based on the available X-ray and radio upper limits. In a wind environment, the allowed parameter space is weakly dependent on the viewing angle θ_v/θ_c. We have fixed $\theta_c = 0.15$ rad, $A_* = 1$, $\varepsilon_e = 0.1$, $\varepsilon_B = 0.01$, and $p = 2.2$. As an example of the impact of decreasing density, we show the allowed parameter space for $A_* = 0.1$ as solid lines (see also Figure 18 in Appendix B).

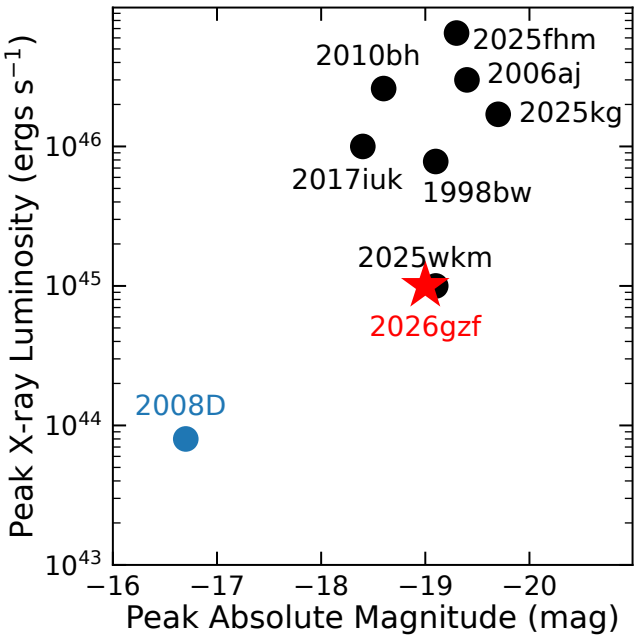

Figure 13. X-ray luminosity vs. peak absolute magnitude of SN shock breakout candidates detected by Swift (GRB 980425/SN 1998bw; GRB 060218/SN 2006aj; XRF 080109/SN 2008D; GRB 100316D/SN 2010bh; GRB 171205A/SN 2017iuk) and the EP (EP250108a/SN 2025kg; EP250827b/SN 2025wkm). EP260321a/SN 2026gzf is shown as a red star (W. Yuan et al. 2026). SN Ic-BL are shown as black circles. SN 2008D, an SN Ib, is shown as a blue circle. Data have been taken from T. J. Galama et al. (1998), A. M. Soderberg et al. (2006, 2008), R. L. C. Starling et al. (2011), Z. Cano et al. (2011), L. Izzo et al. (2019), W. X. Li et al. (2025), J. C. Rastinejad et al. (2025), G. P. Srinivasaragavan et al. (2025a, 2025b), and L. Cotter et al. (2026). This figure is reproduced from J. C. Rastinejad et al. (2025) with the addition of newer EP events (SNe 2025wkm and 2026gzf). Here, we have utilized the dust-corrected absolute magnitudes of SN 2008D and SN 2010bh.

are shown in Figure 12. In a wind environment, the entire surface of the jet decelerates rapidly at small radii (due to the higher density closer to the star), which reduces the dependence of the flux on viewing angle compared with a uniform density medium. Therefore, these results are very weakly dependent on the viewing angle. For these assumed parameters, most specifically the density (see Figure 18 in Appendix B), we find that only low Lorentz factors $\Gamma_0 \lesssim 30$ and low kinetic energies $E_{\rm kin} \lesssim 10^{49}$ erg are allowed for $A_* \gtrsim 1$. If we relax the density to $A_* = 0.1$ (see Figure 12), then the requirement decreases to $\Gamma_0 \lesssim 100$ and $E_{\rm kin} \lesssim 10^{50}$ erg. This implies that if the stellar explosion drove a successful relativistic jet into the surrounding stellar wind, it would have to be extremely weak and mildly relativistic if the environment was typical of those observed for long GRBs. However, if the surrounding density is lower by $>10\times$ than this assumption (i.e., if $A_* \lesssim 0.1$), then we cannot rule out an ultrarelativistic jet ($\Gamma_0 > 100$) with energies of $E_{\rm kin} \lesssim 10^{50}$, significantly reducing the required parameter space, especially for the Lorentz factor. For additional analyses of the presence of a relativistic outflow, see W. Yuan et al. (2026), A. Martin-Carrillo et al. (2026), and J. C. Rastinejad et al. (2026).

4. Discussion

4.1. Origin of the X-Ray Emission

Despite their theoretical ubiquity, detections of the onset of SN shock breakouts are extremely rare and notoriously difficult to catch due to their faint nature, short duration, and largely soft X-ray or ultraviolet emission that lies in a little probed region of parameter space. At high-energy wavelengths, the most convincing example of shock breakout is associated with the SN Ib SN 2008D (P. A. Mazzali et al. 2008; A. M. Soderberg et al. 2008; D. Malesani et al. 2009). Additional, generally accepted, examples of relativistic shock breakout are associated with low-luminosity GRBs, such as GRBs 060218 ($z = 0.0331$), 100316D ($z = 0.0591$), and 171205A ($z = 0.0368$); see, e.g., S. Campana et al. (2006b), G. Ghisellini et al. (2006), R. L. C. Starling et al. (2011), V. D'Elia et al. (2018), and L. Izzo et al. (2019). However, in those cases there is theoretical disagreement over the exact origin of the prompt gamma-ray and X-ray emission in terms of relative contributions from the jet and breakout emission (e.g., E. Waxman et al. 2007; C. M. Irwin & R. A. Chevalier 2016; C. M. Irwin & K. Hotokezaka 2025a). Each of these low-luminosity GRB/shock breakout candidates have been associated with relativistic outflows and SNe Ic-BL, while SN 2008D displayed at most transrelativistic ejecta (A. M. Soderberg et al. 2008) and was associated with an SN Ib.

The prompt high-energy emission of EP260321a is unusual in the context of the known population of nearby SNe Ic-BL with X-ray or gamma-ray triggers (Figures 13 and 14). The EP/WXT spectrum was well described by a soft thermal component with $kT = 132^{+30}_{-21}$ eV and a time-averaged unabsorbed luminosity of $L_{\rm X} = (1.0 \pm 0.3) \times 10^{45}$ erg s^{-1} (W. Yuan et al. 2026). This luminosity is $10\times$ fainter than the peak X-ray luminosities of the nearby low-luminosity GRBs GRB 060218/SN 2006aj (S. Campana et al. 2006a; A. M. Soderberg et al. 2006) and GRB 100316D/SN 2010bh (R. Chornock et al. 2010; Z. Cano et al. 2011;

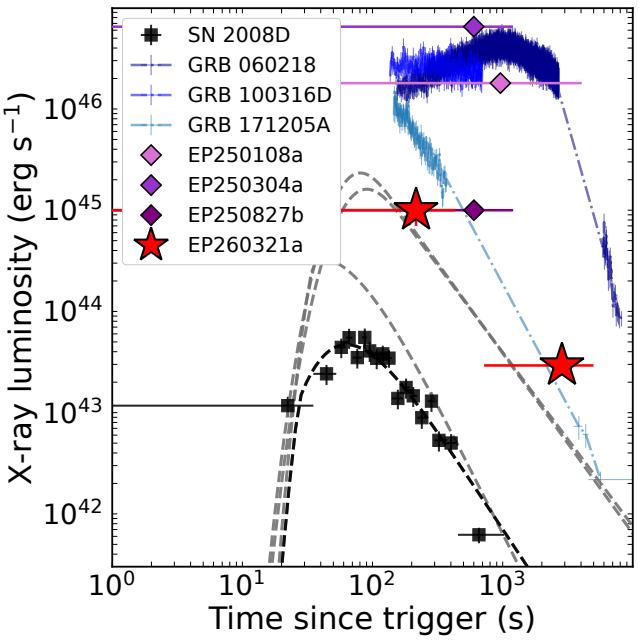

Figure 14. X-ray lightcurves of shock breakout candidates detected by Swift and EP. The EP events are based on time-averaged spectra, and the initial data point for each event is in the 0.5–4 keV band, while all other points (and all Swift events) are in the 0.3–10 keV band. However, the EP events display soft spectra and are unlikely to be very different in a broader energy band. Data have been taken from A. M. Soderberg et al. (2008), H. Sun et al. (2025), W. X. Li et al. (2025), G. P. Srinivasaragavan et al. (2025b), and W. Yuan et al. (2026). Dashed lines represent a compilation of SN Ib and SN Ic-BL shock breakout models from C. L. Fryer et al. (2026). We note that the delay in the start of the GRB lightcurves is due to the slew time of Swift following the gamma-ray triggers.

R. L. C. Starling et al. 2011) and the recent EP SN Ic-BL shock breakout candidates EP250108a/SN 2025kg ($z = 0.176$; R. A. J. Eyles-Ferris et al. 2025; W. X. Li et al. 2025; G. P. Srinivasaragavan et al. 2025a; J. C. Rastinejad et al. 2025) and EP250304a/SN 2025fhm ($z = 0.2$; L. Cotter et al. 2026), see Figure 13. The peak luminosity is the same as reported for the subthreshold EP transient EP250827b/SN 2025wkm ($z = 0.119$; G. P. Srinivasaragavan et al. 2025b). At the same time, the associated SN resides in the typical range of peak[36] optical brightness for SNe Ic-BL associated with both GRBs and FXTs (Figure 13; see also Section 4.2). Thus, EP260321a occupies a region of parameter space in which the SN robustly resembles the energetic SNe Ic-BL explosions associated with GRBs and FXTs, extending the low-luminosity end of the shock breakout population and more comparable to SN 2008D, despite the higher photospheric velocities and absolute magnitude of SN 2026gzf (Figures 4 and 10).

This combination conclusively demonstrates that the luminosity of the high-energy breakout emission is not influenced by the optical luminosity of the SN (Figure 13). Instead, the X-ray output depends sensitively on the structure of the fastest ejecta, the Lorentz factor of the shock, the breakout radius, and the immediate circumstellar environment (see, e.g., C. L. Fryer et al. 2026). Thus, EP260321a represents a lower-luminosity extension of the same family of high-energy shock breakouts previously identified through Swift and EP. This interpretation is also consistent with recent models predicting that the majority of detectable stellar shock breakouts should be substantially fainter than the classical low-luminosity GRBs and therefore most readily discovered by wide-field soft X-ray monitors such as the EP (A. J. Bayless et al. 2022; H. Sun et al. 2022; C. L. Fryer et al. 2026). The location of EP260321a in Figure 13 therefore argues against a direct mapping between SN Ic-BL luminosity and prompt X-ray luminosity, and instead points to a broad luminosity function for high-energy breakout, requiring a more extended distribution of physical parameters at explosion to bridge the gap between SN 2008D and GRB 060218. A broad luminosity function, dominated by fainter breakouts, also provides a more natural explanation for the mismatch between theoretical predictions for the rate of shock breakouts that the EP should detect and the true rate of detected events (see, e.g., H. Sun et al. 2022; C. L. Fryer et al. 2026).

Interestingly, while the duration of the X-ray emission in EP260321a is shorter than in low-luminosity GRBs (Figure 13), it is longer than in SN 2008D and is much longer than the light-crossing time of a Wolf–Rayet star, which is of order 10 s. This may require an asymmetric explosion or a breakout which occurs in dense material outside the star (see C. M. Irwin et al. 2021 for further discussion, and e.g., G. Svirski & E. Nakar 2014a, 2014b). The presence of such extended material is consistent with the progenitor's apparent pre-explosion activity (T.-W. Chen et al. 2026); see also Appendix C.

There are multiple proposed explanations for low-luminosity GRBs and the multicomponent broadband emission observed from GRB 060218-like events; see, e.g., C. M. Irwin & R. A. Chevalier (2016) and C. M. Irwin & K. Hotokezaka (2025b) for an in-depth summary. Leading models include that of mildly relativistic or subrelativistic shock breakout (S. Campana et al. 2006b; A. M. Soderberg et al. 2006; E. Waxman et al. 2007; C. M. Irwin & K. Hotokezaka 2025b), a choked jet (E. Nakar 2015), and models that decouple the gamma-ray emission from the rest of the components, such that the X-rays and gamma rays are produced by a weak jet and the optical emission is produced by the cooling post-breakout ejecta (e.g., C. M. Irwin & R. A. Chevalier 2016). In these models, the multiple components are generally considered to be isotropic, with the exception of jetted gamma-ray emission. As EP260321a does not display gamma-ray emission or low-luminosity GRB-like X-ray or radio emission, and it is noticeably weaker in its overall X-ray luminosity (and spectral shape) than other events of this class (see also W. Yuan et al. 2026), it may favor models that decouple the presence of gamma rays from the shock breakout.

However, it should be noted that GRBs 060218, 100316D, and 171205A were initially detected in gamma rays as roughly constant flux image triggers (see, e.g., A. Lien et al. 2014) by Swift's Burst Alert Telescope (BAT; N. Gehrels et al. 2004; S. D. Barthelmy et al. 2005), as opposed to shorter-duration events like typical GRBs. Using BAT trigger simulations (A. Lien et al. 2014; M. J. Moss et al. 2022, 2026), these events are not detectable by BAT beyond 400 Mpc, which is why these events were all identified at much closer distances of ∼150–260 Mpc and why their observed event rate has not substantially increased over the decades. Therefore, the lack of prompt gamma-ray detection for EP260321a can be due to different causes, such as the current suspended operation status

[36] The peak absolute magnitude refers to the brightness at the SN lightcurve peak at ∼10–20 days post-explosion and not the early shock cooling emission seen in low-luminosity GRBs (e.g., S. Campana et al. 2006a).

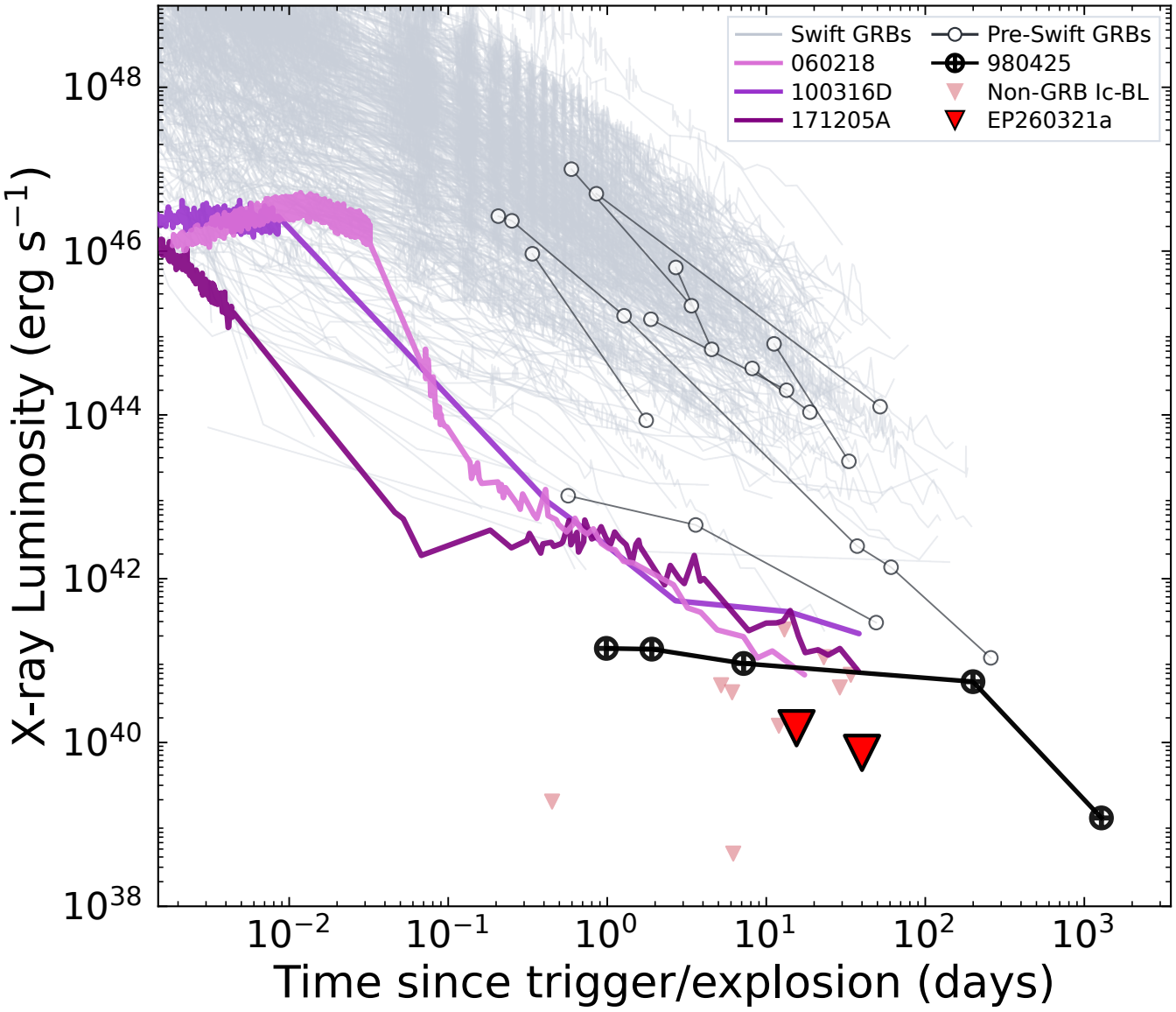

Figure 15. Observer-frame X-ray afterglow (0.3–10 keV) lightcurves of GRBs and FXTs. The X-ray upper limits from Chandra for EP260321a are shown as downward red triangles. For comparison, we show both long and short GRBs (gray) from Swift (P. A. Evans et al. 2007, 2009), and specifically highlight a sample of low-luminosity GRBs. Additional X-ray data for GRBs 060218 and 100316D are compiled from A. M. Soderberg et al. (2006) and R. Margutti et al. (2013a). Pre-Swift GRB and XRF X-ray afterglows are reproduced from E. Pian et al. (1999, 2000, 2004), C. Kouveliotou et al. (2004), A. Tiengo et al. (2004), D. Watson et al. (2004) and references therein. X-ray upper limits for non-GRB-associated SNe Ic-BL (orange downward triangles) were obtained from T. O'Dwyer et al. (2026).

of Swift, and the location of the source on the sky with respect to GRB detectors (e.g., Fermi was in the South Atlantic Anomaly).

Despite these caveats, a main difference between EP260321a and these other events is the lack of an additional power-law component in the X-ray spectrum (W. Yuan et al. 2026), which was observed in both the low-luminosity GRBs that were likely produced by relativistic shock breakout (S. Campana et al. 2006a; R. L. C. Starling et al. 2011; V. D'Elia et al. 2018; L. Izzo et al. 2019) as well as SN 2008D (A. M. Soderberg et al. 2008; M. Modjaz et al. 2009). A power-law component, as opposed to the observed low-kT thermal emission (W. Yuan et al. 2026), would more naturally suggest that gamma-ray emission was possible. Therefore, EP260321a/SN 2026gzf demonstrates that prompt X-ray emission can be produced in the absence of simultaneous gamma rays, more strongly suggesting these components may have had separate origins in nearby low-luminosity GRBs. Alternatively, this may also be simply due to higher Lorentz factor outflows launched by these other events (e.g., C. L. Fryer et al. 2026). We also note that power-law X-ray emission does not necessarily imply the presence of a jet, as it may also be produced by shock breakout under certain conditions (see, e.g, C. M. Irwin & K. Hotokezaka 2025a, 2025b, 2025c). The lack of a power-law component significantly constrains the properties leading to the observed shock breakout emission, and in particular, may require shock velocities that do not significantly exceed $0.1c$ (see, e.g., C. M. Irwin & K. Hotokezaka 2025a, 2025b, 2025c).

4.2. Comparison to GRB-SNe and FXT-SNe

Following the groundbreaking discovery of GRB 980425/SN 1998bw (T. J. Galama et al. 1998), over the last 28 yr there

have been ∼70 identified GRB-SNe of which about half are spectroscopically classified (see, e.g., S. E. Woosley & J. S. Bloom 2006; J. Hjorth & J. S. Bloom 2012; Z. Cano et al. 2017a; G. Finneran et al. 2025b, and references therein), though only about a dozen have high signal-to-noise, multi-epoch spectral sequences. EP260321a/SN 2026gzf is the 16th high-energy (X-ray or gamma-ray) transient associated with an SN Ic-BL within $z < 0.2$, only the 11th within $z < 0.1$, and the fifth closest ever, including being the closest X-ray triggered SN Ic-BL.[37] Thus, the association of SN 2026gzf with EP260321a places it among a small but rapidly growing sample of nearby SNe Ic-BL discovered through prompt high-energy emission.

We have presented a comprehensive investigation placing SN 2026gzf in the context of both GRB-SNe and FXT-SNe, as well as optically selected SNe Ic-BL (F. Taddia et al. 2018, 2019; G. P. Srinivasaragavan et al. 2024). We find an overall good agreement with the general population in terms of lightcurve shape (Figures 2, 3, and 4), absolute magnitude (Figure 4), spectral evolution (Figures 6 and 9), and ejecta velocities (Figures 8 and 10). In Figure 4, we compare the peak magnitude, peak time, and post-peak decline rate of SN 2026gzf to literature samples of GRB-SNe, FXT-SNe, and optically selected SNe Ic-BL. SN 2026gzf peaks at $M_r \approx -19$ mag on a rest-frame timescale of ≈15 days in the r band, with a decline rate of $\Delta m_{15,r} \approx 0.6$ mag, falling in a region of this multidimensional parameter space that is closest to previously known GRB-SNe and FXT-SNe. This is important because the X-ray emission of EP260321a is substantially fainter than that of the low-luminosity GRBs and other EP shock breakout candidates (Figure 13), yet the optical SN itself is not correspondingly faint.

The spectral evolution leads to the same conclusion. The DESI spectrum obtained near optical maximum at $T_0 + 17.7$ days shows broad absorption features characteristic of SNe Ic-BL and closely resembles spectra of the GRB-SNe SN 2006aj, SN 2013dx, and SN 2017iuk at similar phases (Figure 9). The overall spectral morphology and its evolution (Figure 6) are clearly that of a high-velocity stripped-envelope explosion. The match to GRB-SNe is particularly notable because EP260321a was not accompanied by a detected GRB and because its prompt X-ray spectrum was characterized by soft, thermal emission (Q. J. Huang et al. 2026). Thus, the optical spectra identify SN 2026gzf as a member of the energetic SN Ic-BL class, independent of the unusually high-energy properties of EP260321a (Figures 13, 14, and 15).

The velocity evolution further supports this interpretation. In Figure 10, we compare the Fe IIλ5169 and Si IIλ6355 velocities of SN 2026gzf to the SN Ic-BL and GRB-SN sample of G. Finneran et al. (2025a). At the earliest phases, SN 2026gzf shows very high velocities, with both Fe II and Si II indicating material moving at ∼30,000 km s^{-1}. These velocities decline rapidly over the first two weeks and then evolve more slowly, reaching values near the median of the GRB-SN Ic-BL comparison sample around peak light. The early high velocities are most similar to the upper envelope of the GRB-SN population, while the later velocities remain consistent with the broader SN Ic-BL distribution, and are

[37] The previous closest is EP250827b at $z = 0.119$ (G. P. Srinivasaragavan et al. 2025b) followed by EP250108a at $z = 0.176$ (R. A. J. Eyles-Ferris et al. 2025; W. X. Li et al. 2025; J. C. Rastinejad et al. 2025; G. P. Srinivasaragavan et al. 2025a).

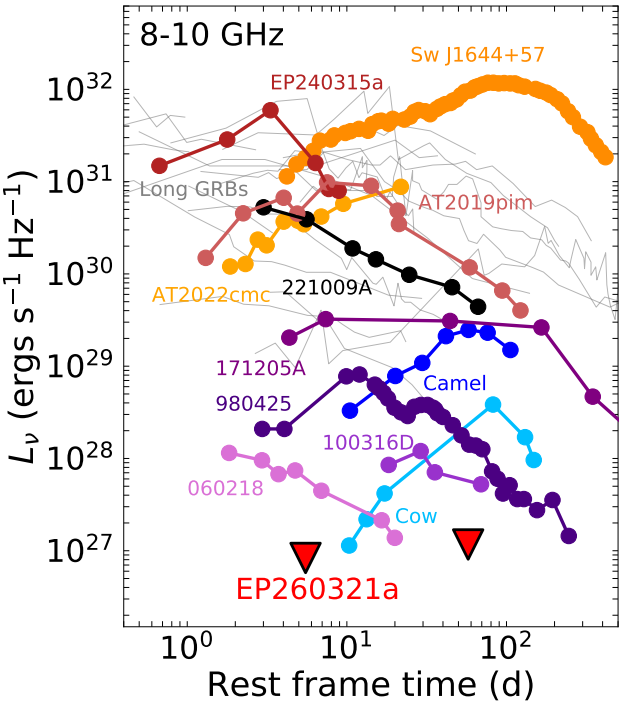

Figure 16. Comparison between the radio upper limits for EP260321a (downward red triangles) versus the radio luminosity of multiple classes of energetic transients, including GRBs (A. M. Soderberg et al. 2006; P. Chandra & D. A. Frail 2012; T. Laskar et al. 2022; D. A. Perley et al. 2025; R. Ricci et al. 2025), jetted tidal disruption events (B. A. Zauderer et al. 2011; I. Andreoni et al. 2022), and fast blue optical transients (A. Y. Q. Ho et al. 2019, 2020; R. Margutti et al. 2019; D. L. Coppejans et al. 2020). The figure is reproduced from B. O'Connor et al. (2025b).

substantially higher than SN 2008D (P. A. Mazzali et al. 2008; D. Malesani et al. 2009).

SN 2026gzf therefore adds to the emerging evidence that stripped-envelope SNe with associated prompt X-ray and gamma-ray emission span a continuum in explosion properties. At one end are classical and low-luminosity GRBs, where a relativistic outflow produces gamma rays and long-lived X-ray emission. At the other end are events like SN 2008D (A. M. Soderberg et al. 2008), where the high-energy emission is best understood as shock breakout from a non-GRB SN Ib explosion. EP260321a/SN 2026gzf lies between these regimes, as while its SN properties agree well with known GRB-SNe, its high-energy emission is dominated by a low-luminosity, thermal X-ray transient that more closely resembles the X-ray emission from SN 2008D (Figures 13 and 14). This makes EP260321a one of the clearest examples that the wide-field soft X-ray survey conducted by the EP is uncovering events at the boundary between ordinary stripped-envelope SNe, relativistic shock breakouts, and failed or weak jet explosions.

4.3. Nature of the SN Power Source

In the collapsar model for GRB-SNe and energetic SNe Ic-BL (S. E. Woosley 1993; A. I. MacFadyen & S. E. Woosley 1999; S. E. Woosley & J. S. Bloom 2006), the formation and longevity of an accretion disk around the remnant black hole provides a physical connection between the relativistic jet and the optical SN. If the SN lightcurve is powered by the decay of ^{56}Ni (primarily produced in the disk wind), the brightness of the SN depends primarily on the

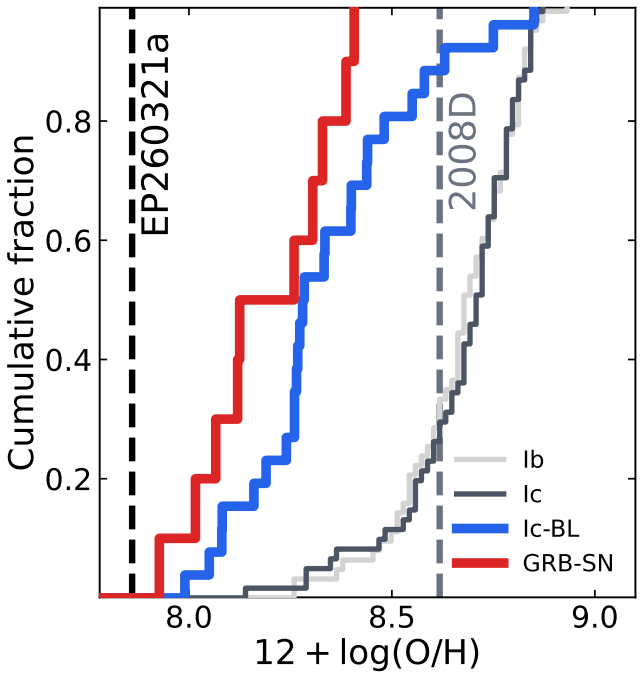

Figure 17. Cumulative distribution of oxygen abundances for low-redshift ($z < 0.2$) SNe Ic-BL without detected GRBs (blue) and GRB-SN Ic-BL events (red), compiled from the PP04 O3N2 (M. Pettini & B. E. J. Pagel 2004) measurements from J. Japelj et al. (2018) and M. Modjaz et al. (2020), and local ($z < 0.025$) SNe Ib and Ic (gray) from M. Modjaz et al. (2011), R. Ganss et al. (2022, 2025) converted to the PP04 O3N2 scale. The metallicity at the explosion sites of EP260321a and SN 2008D is shown as a dashed vertical line.

properties of the disk (Y. Zenati et al. 2020; L. Crosato Menegazzi et al. 2024; C. Dean & R. Fernández 2024). The jet power, and hence the Lorentz factor of the breakout material should also depend on the properties of the disk and we would expect a correlation between the breakout and SN emission. SN 2026gzf presents a challenge to this expectation.

Recent semi-analytic shock breakout calculations show that the X-ray luminosity and duration are sensitive to the energy distribution in the fastest ejecta $E(\Gamma\beta) = E_0\,\Gamma^{-p}$, the maximum Lorentz factor $\Gamma_{\rm max}$, and the effective emitting area (C. L. Fryer et al. 2026). The low X-ray luminosity of EP260321a (Figure 14) relative to relativistic shock breakout events such as GRB 060218/SN 2006aj therefore suggests a lower $\Gamma_{\rm max}$ and less kinetic energy in material with $\Gamma \gtrsim 2$. C. L. Fryer et al. (2026) assumed a maximum Lorentz factor from a weak jet ($\Gamma_{\rm max} = 10$) to a strong jet ($\Gamma_{\rm max} = 100$). Only a subset of the $\Gamma_{\rm max} = 10$ runs match these faint X-ray fluxes (see Figure 14), arguing that the bulk of the ejecta in EP260321a has Lorentz factors below 10 (models with $\Gamma_{\rm max} = 2 - 5$ from C. L. Fryer et al. (2026) can produce better matches to the observed luminosity). The reduced requirements are below the "standard" parameter range in C. L. Fryer et al. (2026) for disk/jet models but on the high end of the standard parameter suite they used for convective engine explosions, requiring a larger exploration over a broader parameter range which we leave to future work. Thus, based on the model gird of C. L. Fryer et al. (2026), EP260321a lies on the edge between disk/jet and neutrino-driven engines.

We note that shock breakout and cooling ejecta only dominates the emission at very early times (T.-W. Chen et al. 2026; A. Martin-Carrillo et al. 2026) In the shock breakout models (C. L. Fryer et al. 2026), the required mass of high Lorentz factor material ($\Gamma > 2$) is very small, less than 0.01–0.1 $M_\odot$. The evolution of the lightcurve after the initial cooling phase probes the nature of the nonrelativistic ejecta (the bulk of the ejecta mass) and requires an additional power source, e.g., ^{56}Ni decay, central engine (fallback accretion or a magnetar) or additional shock interactions. Our simple Arnett model (W. D. Arnett 1982) fit to the bolometric lightcurve (Figure 5) implies a large ^{56}Ni mass of $M_{\rm Ni} = 0.45 \pm 0.02\,M_\odot$, which is consistent with the typical values inferred for GRB-SNe associated to relativistic outflows (Z. Cano et al. 2017a).

Such high ^{56}Ni ejecta masses are possible from models of disk winds and jet outflows, but well beyond the typical ^{56}Ni masses ejected through the neutrino-driven engine (0.05–0.2 $M_\odot$; S. Andrews et al. 2020). The tension between the maximum Lorentz factor and inferred nickel mass suggests either that the jet and disk wind were not tightly coupled in EP260321a, or that the peak optical luminosity does not directly trace the true ^{56}Ni yield. In the first case, the disk may have produced a strong nickel rich wind while the jet was choked before escaping the progenitor. In the second case, additional energy sources, such as shock heating or circumstellar interaction (see, e.g., T.-W. Chen et al. 2026; A. Martin-Carrillo et al. 2026), may have contributed to the bolometric lightcurve, causing a purely radioactive Arnett model to overestimate the nickel mass (A. E. Niblett et al. 2025). Under this interpretation, our inferred $M_{\rm Ni}$ should be regarded as an upper limit to the true ^{56}Ni mass (see, e.g., N. Meza & J. P. Anderson 2020; N. Afsariardchi et al. 2021; Ó. Rodríguez et al. 2023). Despite this caveat, the comparison of our inference of the ^{56}Ni mass with other SNe Ic-BL is still valuable as nickel masses for many SNe Ic-BL and GRB-associated SNe are derived with similar one-zone radioactive models that also neglect possible shock heating (Z. Cano et al. 2017a). EP260321a therefore shows either that there is a weaker correlation between the jet-disk system and the disk wind-produced $M_{\rm Ni}$, or that part of the luminosity commonly attributed to ^{56}Ni in such events may instead arise from a non-radioactive power source (see, e.g., A. E. Niblett et al. 2025; G. P. Srinivasaragavan et al. 2025b). The interpretation can be tested in the future with better models designed to understand the ^{56}Ni production in disks and the disk's connection to the observed shock breakout emission.

4.4. Constraints on a Relativistic Outflow

In contrast to low-luminosity GRBs, EP260321 only displayed prompt X-ray emission and was subsequently undetected by Chandra at $T_0 + 15.4$ and $T_0 + 39.0$ days. These limits are far below the X-ray luminosities of the known low-luminosity GRBs (see Figure 15) at comparable phases. We note that the low-luminosity GRBs 060218, 100316D, and 171205A, shown in Figure 15, are the faintest Swift afterglows and each has X-ray data at the phase of our Chandra observations. The exception being the pre-Swift GRB 980425, which requires a slight extrapolation, though given its lack of evolution to >100 days we consider this to be reasonable. Although the physical origin of the late-time X-ray emission in events such as GRB 060218 and GRB 100316D remains debated (e.g., A. M. Soderberg et al. 2006; R. Margutti et al. 2013b), our Chandra limits show that EP260321a did not produce a comparable long-lived X-ray component. This marks a genuine observational difference

between EP260321a and previously known GRB-SN shock breakout events. More generally, these Chandra limits are capable of excluding all previously known X-ray afterglows of both short and long GRBs, XRFs, and EP FXTs (e.g., L. Cotter et al. 2026) that have a known redshift, with the single exception of GRB 170817A (e.g., R. Margutti et al. 2017; E. Troja et al. 2017). The existing radio limits produce similarly stringent constraints (Figure 16).

The absence of a luminous late-time X-ray or radio counterpart strongly disfavors the presence of a relativistic outflow, as seen in standard GRBs. As discussed in Section 3.4, our Chandra limits, together with available radio upper limits (J. K. Leung et al. 2026), exclude a broad region of parameter space for a relativistic jet propagating into a wind environment, with a very weak dependence on viewing angle. For typical densities $A_* = 1$ (Figure 12), we require both a slower moving, low-energy jet with isotropic-equivalent $E_{\rm kin} < 10^{49}$ erg and Lorentz factor $\Gamma_0 < 30$ at the jet's core. As demonstrated in Figure 12, these results have only a very weak dependence on viewing angle, but a strong dependence on the assumed density (see also Figure 18 in Appendix B) such that for densities below $A_* \lesssim 0.1$ the allowed parameter space greatly relaxes and we would no longer be capable of excluding ultrarelativistic outflows or more energetic jets. Our conclusions are similar to and consistent with the independent analyses of W. Yuan et al. (2026), J. C. Rastinejad et al. (2026), and A. Martin-Carrillo et al. (2026).

We conclude that both a weak jet with an extremely low kinetic energy propagating into a very low density environment or a choked jet whose energy is deposited into a mildly relativistic cocoon could sufficiently suppress the observed gamma-ray and late-time afterglow emission. However, regardless of the interpretation, our deep Chandra limits require that any such component be substantially fainter than the afterglows of known nearby GRB-SNe and FXT-SNe, suggesting the absence of a luminous, relativistic jet. Therefore, not all luminous SNe Ic-BL that display high-energy emission are necessarily associated with relativistic ejecta. Similar conclusions have been drawn for optically selected SNe Ic-BL (see Figure 15; A. Corsi et al. 2023; T. O'Dwyer et al. 2026; G. Schroeder et al. 2025), though each of those lacked any high-energy association.

4.5. Local Environment and Metallicity

The host galaxy of SN 2026gzf is a blue, dwarf galaxy with stellar mass of $\sim 10^9 M_\odot$ (T.-W. Chen et al. 2026; J. C. Rastinejad et al. 2026) that is actively star forming ($\rm SFR_{H\alpha} \approx 0.07\, M_\odot\, yr^{-1}$) and has a subsolar metallicity of $12 + \log({\rm O/H}) \approx 8.2$. This is already a prime environment for the production of an SN Ic-BL progenitor. However, the transient is located 2.5 kpc from the center of the host (Figure 1), and the local environment is most relevant to the progenitor properties (see Section 3.3). The explosion site of EP260321a/SN 2026gzf is actively star forming at a higher rate than the rest of the host galaxy with an $\rm SFR_{H\alpha} \approx 0.2\, M_\odot\, yr^{-1}$. Additionally, the location of the transient has a lower metallicity than the rest of the host, with $12 + \log({\rm O/H}) \approx 7.9$; see Figure 11. This trend is commonly observed in low-z GRBs, such that the local environment is less metal-enriched compared to the rest of the galaxy (E. M. Levesque et al. 2011; C. C. Thöne et al. 2014, 2021, 2024; T. Krühler et al. 2015, 2017; Z. Cano et al. 2017b; L. Izzo et al. 2017; M. J. MichałowskI et al. 2018; M. Tanga et al. 2018; A. Melandri et al. 2019).

The lack of metal enrichment in the local environment is consistent with observations of GRB-associated SNe Ic-BL (e.g., E. M. Levesque et al. 2010a, 2010b; T. Krühler et al. 2015) and non-GRB-associated SNe Ic-BL discovered through untargeted optical surveys (J. Japelj et al. 2018; M. Modjaz et al. 2020). In Figure 17, we compare the metallicity at the explosion site of EP260321a/SN 2026gzf to these two populations of low-redshift $z < 0.2$ SNe Ic-BL with and without associated GRBs using the O3N2 calibration of M. Pettini & B. E. J. Pagel (2004). The local environment of EP260321a is clearly extremely metal-poor, and one of the lowest-metallicity environments observed for an SN Ic-BL both in general and, in particular, for an SNe Ic-BL without an associated GRB. The metallicity also differs significantly from the environments of SNe Ib and Ic (see Figure 17; R. Ganss et al. 2022, 2025), such as SN 2008D (C. C. Thöne et al. 2009; M. Modjaz et al. 2011). As EP260321a both lacked a GRB association and occurred in such a low-metallicity environment, it strongly suggests that metallicity cannot be the only factor in producing a progenitor star population of "collapsars" (S. E. Woosley 1993; A. I. MacFadyen & S. E. Woosley 1999) capable of launching relativistic outflows (see also C. Wolf & P. Podsiadlowski 2007; P. Schady et al. 2015; M. M. Briel et al. 2025; P. Disberg et al. 2025, and references therein).

We note that our results are in agreement with the analysis of A. Martin-Carrillo et al. (2026) and T.-W. Chen et al. (2026), who likewise find this to be an extremely low-metallicity environment. We must note however, as stated in Section 3.3, that the derived values of O3N2 and N2 that lead to this metallicity lie outside of the range of values used to define the oxygen abundance calibrations and additionally that these calibrations have systematic uncertainties of 0.1–0.2 dex (see M. Pettini & B. E. J. Pagel 2004; R. A. Marino et al. 2013). This is of course always the case when extending to such low metallicity, and while the exact value of $12 + \log({\rm O/H})$ may therefore be uncertain, the derived O3N2 and N2 strongly point to an extremely metal-poor local environment of SN 2026gzf that is different from the bulk of the SN Ic-BL and Ibc populations (Figure 17).

5. Conclusions

We have presented a comprehensive photometric ($ugrizJK_s$) and spectroscopic observing campaign of EP260321a/SN 2026gzf over the first 55 days of its evolution using FTW, DECam, DESI, SALT, and HET. Our photometric observations with FTW begin 10 hr after the detection of the X-ray shock breakout emission. We subsequently observe the rising emission from the SN and our spectral observations starting at 3.3 days after explosion capture high-velocity $\sim$30,000 km s^{-1} ejecta that we observe to decelerate and produce numerous broad absorption features typical of SNe Ic-BL. We find that SN 2026gzf is a typical SN Ic-BL in all respects, from its lightcurve and spectral evolution to its overall bolometric luminosity.

We additionally obtained deep X-ray imaging with the CXO at 15 and 39 days after explosion and radio imaging with the Very Large Array at 60 days. Combined with the unprecedented sensitivity of Chandra and the nearby distance of EP260321a at 158 Mpc, our observations can exclude the afterglow of all previously known GRBs (that have a redshift),

with the singular exception of the exceptional off-axis binary neutron star merger GW170817 (E. Troja et al. 2017; R. Margutti et al. 2018), down to an X-ray luminosity of 10^{40} erg s^{-1} between 15 and 60 days after explosion. We apply these constraints to exclude a collimated relativistic outflow with both high kinetic energies and high Lorentz factors, requiring instead $E_{\rm kin} < 10^{49}$ erg and $\Gamma_0 < 30$ for a typical stellar wind density of $A_* \gtrsim 1$. This requirement can be strongly relaxed for lower assumed densities, such that for $A_* = 0.1$ the constraints relax to $E_{\rm kin} < 10^{50}$ erg and $\Gamma_0 < 100$. Therefore, while we cannot fully exclude all possible afterglow parameters, we can conclude that observationally any afterglow arising from this event differs from past observations of low-luminosity GRBs.

We interpret EP260321a as a low-luminosity, thermally dominated shock breakout event associated with an otherwise typical energetic SN Ic-BL. The event bridges SN 2008D-like X-ray shock breakout and the SNe Ic-BL associated with low-luminosity GRBs. Unlike SN 2008D, however, the associated SN Ic-BL with higher ejecta velocities, and unlike the classical nearby low-luminosity GRBs, EP260321a lacks both a gamma-ray detection and a late-time X-ray or radio afterglow. This combination is naturally explained if EP260321a was produced by a mildly relativistic shock breakout caused by a weak jet/cocoon in which the fastest ejecta produced the observed soft X-rays but did not generate either a bright X-ray or radio afterglow or substantial gamma-ray emitting material along the line of sight.

While observations of shock breakout events have been limited over the last three decades due to the requirement of serendipitous timing of the explosion with observations from narrow-field instruments (e.g., A. M. Soderberg et al. 2008; D. Alp & J. Larsson 2020), the launch of the EP (W. Yuan et al. 2015, 2022, 2025) in 2024 January has enabled a drastic increase in their rate of discovery over the last few years. The launch of the BlackCAT mission (J. M. Colosimo et al. 2024; A. D. Falcone et al. 2024) and upcoming wide-field ultraviolet missions, ULTRASAT (I. Sagiv et al. 2014; Y. Shvartzvald et al. 2024) and UVEX (S. R. Kulkarni et al. 2021), will aid in driving a shock breakout revolution and expand our understanding of the deaths of massive stars and their pre-explosion mass loss and eruptions.

Acknowledgments

The authors acknowledge the anonymous referee for their careful reading of the manuscript and for their constructive comments that led to a clearer presentation of our results.

B.O. and X.J.H. thank Moses Mogotsi, Lee Townsend, and Danièl Groenewald for approving a SALT DDT request and for assistance in obtaining the observations. B.O. acknowledges the staff of the CXO, including Pat Slane, Dan Schwartz, Jack Steiner, and Vinay Kashyap, for approving and rapidly scheduling the Chandra observations.

B.O. is supported by the McWilliams Postdoctoral Fellowship in the McWilliams Center for Cosmology and Astrophysics at Carnegie Mellon University. J.H. acknowledges support from NASA under award No. 80GSFC24M0006. C.M. I. is supported by the JST FOREST Program (JPMJFR2136) and the JSPS Grant-in-Aid for Scientific Research (20H05639, 20H00158, 23H01169, 23H04900, 26K07149). Support was provided by Schmidt Sciences, LLC for K. Malanchev. A.F. was funded by the European Union ERC-2022-STG—BOOTES—101076343. Views and opinions expressed are however those of the author(s) only and do not necessarily reflect those of the European Union or the European Research Council Executive Agency. Neither the European Union nor the granting authority can be held responsible for them.

This work used resources on the Vera Cluster at the Pittsburgh Supercomputing Center (PSC). Vera is a dedicated cluster for the McWilliams Center for Cosmology and Astrophysics at Carnegie Mellon University. We thank the PSC staff for their support of the Vera Cluster.

Support for this work was provided by NASA through Chandra award No. GO6-27037X, issued by the CXC, which is operated by the Smithsonian Astrophysical Observatory for and on behalf of NASA under contract NAS8-03060.

The scientific results reported in this article are based on observations made by CXO. This research has made use of data obtained from the Chandra Data Archive provided by CXC. This Letter employs a list of Chandra datasets, obtained by the CXO, contained in the Chandra Data Collection DOI: 10.25574/cdc.617. This research has made use of software provided by CXC in the application package CIAO.

This Letter contains data obtained at the Wendelstein Observatory of the Ludwig-Maximilians University Munich. Funded by the Deutsche Forschungsgemeinschaft (DFG, German Research Foundation) under Germany's Excellence Strategy—EXC-2094/2—390783311.

Some of the observations reported in this Letter were obtained with SALT.

This material is based upon work supported by the US Department of Energy (DOE), Office of Science, Office of High-Energy Physics, under Contract No. DE-AC02–05CH11231, and by the National Energy Research Scientific Computing Center, a DOE Office of Science User Facility under the same contract. Additional support for DESI was provided by the US National Science Foundation (NSF), Division of Astronomical Sciences under Contract No. AST-0950945 to the NSF's National Optical-Infrared Astronomy Research Laboratory; the Science and Technology Facilities Council of the United Kingdom; the Gordon and Betty Moore Foundation; the Heising–Simons Foundation; the French Alternative Energies and Atomic Energy Commission (CEA); the National Council of Humanities, Science and Technology of Mexico (CONAHCYT); the Ministry of Science, Innovation and Universities of Spain (MICIU/AEI/10.13039/501100011033), and by the DESI Member Institutions: https://www.desi.lbl.gov/collaborating-institutions. The authors are honored to be permitted to conduct scientific research on I'oligam Du'ag (Kitt Peak), a mountain with particular significance to the Tohono O'odham Nation. Any opinions, findings, and conclusions or recommendations expressed in this material are those of the author(s) and do not necessarily reflect the views of the US NSF, the US DOE, or any of the listed funding agencies.

This material is based upon work supported in part by the National Science Foundation through Cooperative Agreements AST-1258333 and AST-2241526 and Cooperative Support Agreements AST-1202910 and 2211468 managed by the Association of Universities for Research in Astronomy (AURA), and the Department of Energy under Contract No. DE-AC02-76SF00515 with the SLAC National Accelerator Laboratory managed by Stanford University. Additional Rubin Observatory funding comes from private donations, grants to

universities, and in-kind support from LSST-DA Institutional Members.

Based on observations obtained with the Samuel Oschin Telescope 48 inch and the 60 inch Telescope at the Palomar Observatory as part of the ZTF project. ZTF is supported by the NSF under grant Nos. AST-1440341, AST-2034437, and currently Award AST-2407588. ZTF receives additional funding from the ZTF partnership. Current members include Caltech, USA; Caltech/IPAC, USA; University of Maryland, USA; University of California, Berkeley, USA; University of Wisconsin at Milwaukee, USA; Cornell University, USA; Drexel University, USA; University of North Carolina at Chapel Hill, USA; Institute of Science and Technology, Austria; National Central University, Taiwan, and OKC, University of Stockholm, Sweden. Operations are conducted by Caltech's Optical Observatory (COO), Caltech/IPAC, and the University of Washington at Seattle, USA.

The Babamul alerts broker and BOOM software infrastructure (T. Jegou du Laz et al. 2026) is codeveloped by the California Institute of Technology and the University of Minnesota. This work acknowledges support from the National Science Foundation through AST award No. 2432476 (PI: Kasliwal; co-PI: Coughlin) and leverages experience from the ZTF (co-PIs: Graham and Kasliwal).

This research is based on data obtained from the Astro Data Archive at NSF NOIRLab. NOIRLab is managed by AURA under a cooperative agreement with the US National Science Foundation. This project used data obtained with the DECam, which was constructed by the DES Collaboration. Funding for the DES projects has been provided by the US DOE, the US NSF, the Ministry of Science and Education of Spain, the Science and Technology Facilities Council of the United Kingdom, the Higher Education Funding Council for England, the National Center for Supercomputing Applications at the University of Illinois at Urbana-Champaign, the Kavli Institute of Cosmological Physics at the University of Chicago, Center for Cosmology and Astro-Particle Physics at the Ohio State University, the Mitchell Institute for Fundamental Physics and Astronomy at Texas A&M University, Financiadora de Estudos e Projetos, Fundacao Carlos Chagas Filho de Amparo, Financiadora de Estudos e Projetos, Fundacao Carlos Chagas Filho de Amparo a Pesquisa do Estado do Rio de Janeiro, Conselho Nacional de Desenvolvimento Cientifico e Tecnologico and the Ministerio da Ciencia, Tecnologia e Inovacao, the Deutsche Forschungsgemeinschaft and the Collaborating Institutions in the DES. The Collaborating Institutions are Argonne National Laboratory, the University of California at Santa Cruz, the University of Cambridge, Centro de Investigaciones Energeticas, Medioambientales y Tecnologicas-Madrid, the University of Chicago, University College London, the DES-Brazil Consortium, the University of Edinburgh, the Eidgenossische Technische Hochschule (ETH) Zurich, Fermi National Accelerator Laboratory, the University of Illinois at Urbana-Champaign, the Institut de Ciencies de l'Espai (IEEC/CSIC), the Institut de Fisica d'Altes Energies, Lawrence Berkeley National Laboratory, the Ludwig Maximilians Universitat Munchen and the associated Excellence Cluster Universe, the University of Michigan, NSF NOIRLab, the University of Nottingham, the Ohio State University, the University of Pennsylvania, the University of Portsmouth, SLAC National Accelerator Laboratory, Stanford University, the University of Sussex, and Texas A&M University.

This paper contains data from observations obtained with HET, which is a joint project of the University of Texas at Austin, the Pennsylvania State University, Ludwig-Maximilians-Universität München, and Georg-August Universität Göttingen. The HET is named in honor of its principal benefactors, William P. Hobby and Robert E. Eberly. We acknowledge the Texas Advanced Computing Center (TACC) at The University of Texas at Austin for providing high-performance computing, visualization, and storage resources that have contributed to the results reported within this paper. The LRS2 was developed and funded by the University of Texas at Austin, McDonald Observatory, Department of Astronomy, and Pennsylvania State University. We thank the Leibniz-Institut für Astrophysik Potsdam (AIP) and the Institut für Astrophysik Göttingen (IAG) for their contributions to the construction of the IFUs.

The National Radio Astronomy Observatory is a facility of the National Science Foundation operated under cooperative agreement by Associated Universities, Inc.

This work made use of data supplied by the UK Swift Science Data Centre at the University of Leicester. This research has made use of the XRT Data Analysis Software (XRTDAS) developed under the responsibility of the ASI Science Data Center (ASDC), Italy. This research has made use of data and/or software provided by the High Energy Astrophysics Science Archive Research Center (HEASARC), which is a service of the Astrophysics Science Division at NASA/GSFC. This research has made use of the Astrophysics Data System, funded by NASA under Cooperative Agreement 80NSSC21M00561.

Facilities: WO:2m, Mayall, SALT, HET, Blanco, PO:1.2m, Rubin, CXO.

Software: `Astropy` (Astropy Collaboration et al. 2018, 2022), `SFFT` (L. Hu et al. 2022), `AstrOmatic` (E. Bertin & S. Arnouts 1996; E. Bertin 2006, 2010; E. Bertin et al. 2002), `XSPEC` (K. A. Arnaud 1996), `CIAO` (A. Fruscione et al. 2006), `HEASoft` (NASA High Energy Astrophysics Science Archive Research Center (HEASARC) 2014), `CASA` (CASA Team et al. 2022), `HAFFET` (S. Yang & J. Sollerman 2023), `VegasAfterglow` (Y. Wang et al. 2026).

Appendix A
Log of Observations

In Tables 1, 2, and 3, we present a log of all photometric and spectroscopic observations obtained and analyzed in this work.

Table 1
Log of Photometry of EP260321a/SN 2026gzf Obtained with FTW and DECam in This Work

Start Time (UT)	ΔT (days)	Exposure (s)	Telescope	Filter	AB Magnitude
2026-03-21T22:29:50	0.45	5400	FTW	*i*	20.93 ± 0.08
2026-03-21T22:29:50	0.45	5400	FTW	*r*	20.41 ± 0.01
2026-03-21T22:30:08	0.45	5092	FTW	*J*	20.69 ± 0.26
2026-03-23T20:13:21	2.34	2340	FTW	*i*	18.67 ± 0.01
2026-03-23T20:13:21	2.34	2340	FTW	*r*	18.38 ± 0.01
2026-03-23T20:13:40	2.34	2207	FTW	*J*	19.10 ± 0.06
2026-03-24T19:12:49	3.29	1697	FTW	*J*	18.69 ± 0.05
2026-03-24T19:49:19	3.32	1464	FTW	*Ks*	19.40 ± 0.27
2026-03-25T02:32:44	3.59	70	DECam	*g*	17.80 ± 0.01
2026-03-25T02:36:21	3.59	110	DECam	*i*	18.11 ± 0.01
2026-03-25T02:38:40	3.59	90	DECam	*z*	18.41 ± 0.01
2026-03-28T01:47:50	6.55	70	DECam	*g*	17.24 ± 0.01
2026-03-28T01:49:29	6.56	90	DECam	*r*	17.40 ± 0.01
2026-03-28T01:51:28	6.56	110	DECam	*i*	17.53 ± 0.01
2026-03-28T01:53:47	6.56	90	DECam	*z*	17.74 ± 0.01
2026-03-30T03:28:12	8.62	90	DECam	*r*	17.21 ± 0.01
2026-03-30T03:30:10	8.63	110	DECam	*i*	17.36 ± 0.01
2026-03-30T03:32:29	8.63	90	DECam	*z*	17.48 ± 0.01
2026-03-31T01:58:20	9.56	70	DECam	*g*	17.05 ± 0.01
2026-03-31T02:01:57	9.56	110	DECam	*i*	17.30 ± 0.01
2026-03-31T02:04:17	9.57	90	DECam	*z*	17.39 ± 0.01
2026-04-03T02:08:51	12.57	70	DECam	*g*	17.10 ± 0.01
2026-04-03T02:12:28	12.57	110	DECam	*i*	17.22 ± 0.01
2026-04-03T02:14:45	12.57	90	DECam	*z*	17.20 ± 0.01
2026-04-04T23:54:58	14.48	360	FTW	*g*	17.38 ± 0.04
2026-04-04T23:54:58	14.48	1080	FTW	*z*	17.11 ± 0.02
2026-04-06T01:33:58	15.54	70	DECam	*g*	17.31 ± 0.01
2026-04-06T01:35:37	15.55	90	DECam	*r*	17.08 ± 0.01
2026-04-06T01:37:36	15.55	110	DECam	*i*	17.21 ± 0.01
2026-04-06T01:39:54	15.55	90	DECam	*z*	17.06 ± 0.01
2026-04-07T20:47:42	17.38	1620	FTW	*i*	17.20 ± 0.01
2026-04-07T20:47:42	17.38	1620	FTW	*r*	16.99 ± 0.01
2026-04-07T20:58:58	17.39	1260	FTW	*g*	17.52 ± 0.01
2026-04-07T20:58:58	17.39	3240	FTW	*z*	17.03 ± 0.01
2026-04-07T21:47:36	17.40	900	FTW	*u*	19.42 ± 0.11
2026-04-08T01:20:08	17.54	70	DECam	*g*	17.52 ± 0.01
2026-04-08T01:23:47	17.54	110	DECam	*i*	17.22 ± 0.01
2026-04-08T01:26:07	17.54	90	DECam	*z*	17.02 ± 0.01
2026-04-08T19:00:20	18.31	1620	FTW	*i*	17.17 ± 0.01
2026-04-08T19:00:20	18.31	1440	FTW	*r*	17.05 ± 0.01
2026-04-08T19:11:18	18.31	1440	FTW	*g*	17.63 ± 0.01
2026-04-08T19:11:18	18.31	3240	FTW	*z*	17.02 ± 0.01
2026-04-08T19:28:36	18.32	1440	FTW	*u*	19.57 ± 0.10
2026-04-11T18:53:28	21.27	1080	FTW	*z*	17.08 ± 0.01
2026-04-11T19:04:02	21.28	360	FTW	*u*	19.90 ± 0.16
2026-04-11T19:15:13	21.29	720	FTW	*i*	17.23 ± 0.01
2026-04-11T19:15:13	21.28	360	FTW	*r*	17.09 ± 0.01
2026-04-11T19:24:08	21.29	360	FTW	*g*	17.81 ± 0.01
2026-04-15T01:12:14	24.53	70	DECam	*g*	18.24 ± 0.01
2026-04-15T01:15:50	24.53	110	DECam	*i*	17.35 ± 0.01
2026-04-15T01:18:08	24.53	90	DECam	*z*	17.09 ± 0.01
2026-04-15T20:11:36	25.33	720	FTW	*z*	17.17 ± 0.01
2026-04-15T20:35:53	25.35	960	FTW	*i*	17.36 ± 0.01
2026-04-15T20:35:53	25.34	300	FTW	*r*	17.29 ± 0.02
2026-04-15T20:50:56	25.36	660	FTW	*g*	18.33 ± 0.01
2026-04-16T19:12:39	26.28	1080	FTW	*z*	17.28 ± 0.01
2026-04-16T19:35:59	26.30	720	FTW	*i*	17.36 ± 0.01
2026-04-16T19:45:44	26.31	360	FTW	*g*	18.37 ± 0.02
2026-04-17T20:37:54	27.35	900	FTW	*u*	20.63 ± 0.32
2026-04-17T20:37:54	27.36	2160	FTW	*z*	17.22 ± 0.01
2026-04-17T21:11:17	27.38	1440	FTW	*i*	17.44 ± 0.01
2026-04-17T21:11:17	27.38	720	FTW	*r*	17.40 ± 0.01
2026-04-17T21:20:12	27.39	720	FTW	*g*	18.45 ± 0.01

Table 1
(Continued)

Start Time (UT)	ΔT (days)	Exposure (s)	Telescope	Filter	AB Magnitude
2026-04-18T00:26:12	27.50	70	DECam	*g*	18.46 ± 0.01
2026-04-18T00:29:47	27.50	110	DECam	*i*	17.49 ± 0.01
2026-04-18T00:32:06	27.50	90	DECam	*z*	17.20 ± 0.01
2026-04-18T20:02:05	28.32	1260	FTW	*u*	20.65 ± 0.33
2026-04-18T20:09:08	28.33	900	FTW	*z*	17.33 ± 0.01
2026-04-18T20:23:47	28.33	240	FTW	*r*	17.39 ± 0.01
2026-04-18T20:44:38	28.34	240	FTW	*i*	17.47 ± 0.01
2026-04-18T20:48:12	28.35	240	FTW	*g*	18.55 ± 0.01
2026-04-22T19:09:35	32.33	5400	FTW	*z*	17.47 ± 0.01
2026-04-22T19:09:51	32.33	5092	FTW	*J*	17.40 ± 0.01
2026-04-22T19:48:31	32.32	1440	FTW	*u*	20.82 ± 0.31
2026-04-22T20:03:43	32.35	1440	FTW	*i*	17.66 ± 0.01
2026-04-22T20:03:43	32.34	720	FTW	*r*	17.63 ± 0.01
2026-04-22T20:03:58	32.35	1273	FTW	*Ks*	18.31 ± 0.08
2026-04-22T20:14:39	32.35	720	FTW	*g*	18.77 ± 0.01
2026-04-24T20:04:36	34.32	371	FTW	*z*	17.56 ± 0.01
2026-04-24T20:11:08	34.33	371	FTW	*Ks*	18.46 ± 0.11
2026-04-24T20:41:45	34.34	371	FTW	*r*	17.77 ± 0.01
2026-04-24T20:47:59	34.35	371	FTW	*i*	17.71 ± 0.01
2026-04-26T21:19:40	36.37	849	FTW	*J*	17.57 ± 0.02
2026-04-26T21:38:28	36.39	637	FTW	*Ks*	18.44 ± 0.14
2026-05-05T20:01:32	45.32	720	FTW	*i*	18.24 ± 0.01
2026-05-05T20:01:32	45.32	720	FTW	*r*	18.14 ± 0.01
2026-05-05T20:01:45	45.32	679	FTW	*J*	18.00 ± 0.05
2026-05-09T19:45:12	49.31	900	FTW	*i*	18.34 ± 0.01
2026-05-09T19:45:12	49.31	900	FTW	*r*	18.41 ± 0.01
2026-05-09T19:45:17	49.31	903	FTW	*J*	18.14 ± 0.05
2026-05-09T20:03:58	49.32	720	FTW	*g*	19.36 ± 0.02
2026-05-09T20:03:58	49.32	720	FTW	*z*	18.02 ± 0.02
2026-05-09T20:04:02	49.32	723	FTW	*Ks*	>18.74
2026-05-17T20:21:32	57.33	482	FTW	*Ks*	>19.14

Note. Times ΔT are given relative to the EP trigger. The photometry has not been corrected for Galactic reddening $E(B - V) = 0.02$ mag (E. F. Schlafly & D. P. Finkbeiner 2011).

(This table is available in its entirety in machine-readable form in the online article.)

Table 2
Log of Public Photometry of EP260321a/SN 2026gzf Obtained by Rubin/LSST (Ž. Ivezić et al. 2019) and ZTF (E. C. Bellm et al. 2018)

Start Time (UT)	ΔT (days)	Telescope	Filter	AB Magnitude
2026-03-22T07:12:13	0.78	ZTF	r	19.90 ± 0.18
2026-03-22T07:35:25	0.80	ZTF	g	19.70 ± 0.18
2026-03-26T05:04:13	4.69	ZTF	r	17.61 ± 0.05
2026-03-26T06:27:25	4.75	ZTF	i	17.84 ± 0.09
2026-03-26T07:43:20	4.80	ZTF	g	17.62 ± 0.06
2026-03-27T03:53:42	5.64	ZTF	r	17.45 ± 0.05
2026-03-27T04:40:42	5.67	ZTF	g	17.38 ± 0.05
2026-03-27T05:52:30	5.72	ZTF	i	17.63 ± 0.07
2026-04-02T04:46:20	11.68	ZTF	i	17.20 ± 0.04
2026-04-02T05:36:23	11.71	ZTF	r	17.02 ± 0.06
2026-04-05T04:02:34	14.65	ZTF	r	16.98 ± 0.04
2026-04-06T00:29:23	15.50	Rubin	r	17.01 ± 0.01
2026-04-06T00:33:38	15.50	Rubin	z	17.07 ± 0.01
2026-04-06T03:43:42	15.63	Rubin	i	17.20 ± 0.01
2026-04-07T03:27:01	16.62	Rubin	i	17.19 ± 0.01
2026-04-07T03:54:24	16.64	ZTF	i	17.18 ± 0.08
2026-04-07T04:05:27	16.65	ZTF	r	16.99 ± 0.05
2026-04-09T01:42:28	18.55	Rubin	g	17.67 ± 0.01
2026-04-09T01:45:33	18.55	Rubin	i	17.23 ± 0.01
2026-04-09T04:05:02	18.65	ZTF	r	16.98 ± 0.06
2026-04-09T05:05:00	18.69	ZTF	g	17.66 ± 0.07
2026-04-10T04:57:21	19.69	ZTF	i	17.20 ± 0.05
2026-04-10T05:04:20	19.69	ZTF	g	17.75 ± 0.06
2026-04-11T01:48:16	20.55	Rubin	i	17.23 ± 0.01
2026-04-11T02:59:46	20.60	Rubin	g	17.86 ± 0.01
2026-04-11T03:00:27	20.60	Rubin	g	17.87 ± 0.01
2026-04-11T04:08:01	20.65	Rubin	i	17.22 ± 0.01
2026-04-12T01:33:59	21.54	Rubin	u	19.68 ± 0.02
2026-04-12T01:37:30	21.55	Rubin	r	17.11 ± 0.01
2026-04-12T01:41:01	21.55	Rubin	z	17.12 ± 0.01
2026-04-13T00:04:50	22.48	Rubin	u	19.84 ± 0.02
2026-04-13T01:21:55	22.54	Rubin	i	17.27 ± 0.01
2026-04-13T01:25:25	22.54	Rubin	u	19.84 ± 0.02
2026-04-14T01:26:31	23.54	Rubin	r	17.14 ± 0.01
2026-04-14T01:30:03	23.54	Rubin	u	19.95 ± 0.02
2026-04-15T03:01:11	24.60	Rubin	i	17.33 ± 0.01
2026-04-15T03:01:51	24.61	Rubin	i	17.32 ± 0.01
2026-04-16T04:24:29	25.66	ZTF	i	17.37 ± 0.06
2026-04-16T04:33:35	25.67	ZTF	r	17.27 ± 0.06
2026-04-16T06:45:25	25.76	ZTF	g	18.47 ± 0.10
2026-04-17T06:44:31	26.76	ZTF	r	17.35 ± 0.06
2026-04-20T03:42:01	29.63	ZTF	g	18.63 ± 0.12
2026-04-20T04:04:45	29.65	ZTF	r	17.46 ± 0.04
2026-04-21T00:39:56	30.51	Rubin	i	17.60 ± 0.01
2026-04-21T00:40:37	30.51	Rubin	i	17.59 ± 0.01
2026-04-21T00:44:13	30.51	Rubin	u	20.62 ± 0.02
2026-04-21T00:45:01	30.51	Rubin	u	20.57 ± 0.02
2026-04-21T06:56:32	30.77	ZTF	g	18.66 ± 0.13
2026-04-22T01:59:46	31.56	Rubin	r	17.63 ± 0.01
2026-04-24T03:52:48	33.64	ZTF	i	17.68 ± 0.08
2026-04-25T04:26:18	34.66	ZTF	g	18.96 ± 0.20
2026-04-25T05:07:58	34.69	ZTF	r	17.91 ± 0.11
2026-04-29T04:24:56	38.66	ZTF	i	17.97 ± 0.09
2026-04-30T00:03:48	39.48	Rubin	z	17.79 ± 0.01
2026-04-30T00:11:28	39.49	Rubin	r	18.04 ± 0.01
2026-04-30T04:05:09	39.65	ZTF	i	17.97 ± 0.09
2026-04-30T06:37:46	39.76	ZTF	r	18.04 ± 0.13
2026-05-01T02:13:55	40.57	Rubin	g	19.16 ± 0.01
2026-05-01T02:14:36	40.57	Rubin	g	19.14 ± 0.01
2026-05-02T01:32:03	41.54	Rubin	r	18.09 ± 0.01
2026-05-02T01:34:43	41.54	Rubin	z	17.89 ± 0.01
2026-05-02T01:37:23	41.55	Rubin	r	18.10 ± 0.01
2026-05-02T01:40:05	41.55	Rubin	z	17.89 ± 0.01
2026-05-02T01:54:00	41.56	Rubin	z	17.89 ± 0.01
2026-05-02T04:09:19	41.65	ZTF	g	19.22 ± 0.21
2026-05-02T06:30:10	41.75	ZTF	r	18.08 ± 0.12
2026-05-03T04:02:26	42.65	ZTF	g	19.19 ± 0.22
2026-05-07T03:56:16	46.64	ZTF	i	18.32 ± 0.09
2026-05-07T04:55:06	46.68	ZTF	r	18.21 ± 0.08
2026-05-07T06:07:56	46.73	ZTF	g	19.35 ± 0.16
2026-05-08T04:07:28	47.65	ZTF	r	18.28 ± 0.09
2026-05-08T04:39:09	47.67	ZTF	g	19.44 ± 0.16
2026-05-10T04:26:36	49.66	ZTF	r	18.37 ± 0.07
2026-05-10T05:00:37	49.69	ZTF	g	19.45 ± 0.08
2026-05-12T00:03:22	51.48	Rubin	r	18.43 ± 0.01
2026-05-12T23:35:53	52.46	Rubin	u	21.36 ± 0.05
2026-05-12T23:37:33	52.46	Rubin	u	21.36 ± 0.05
2026-05-16T23:40:26	56.47	Rubin	g	19.54 ± 0.01
2026-05-16T23:44:26	56.47	Rubin	u	21.42 ± 0.05
2026-05-17T23:56:03	57.48	Rubin	u	21.58 ± 0.05
2026-05-17T23:56:53	57.48	Rubin	u	21.51 ± 0.05
2026-05-17T23:57:58	57.48	Rubin	u	21.53 ± 0.06
2026-05-18T00:02:29	57.48	Rubin	r	18.57 ± 0.01
2026-05-18T23:35:12	58.46	Rubin	g	19.58 ± 0.01
2026-05-18T23:35:53	58.46	Rubin	g	19.59 ± 0.01
2026-05-18T23:38:53	58.46	Rubin	u	21.39 ± 0.05
2026-05-19T23:50:44	59.47	Rubin	u	21.62 ± 0.06
2026-05-19T23:51:32	59.47	Rubin	u	21.46 ± 0.06
2026-05-25T23:29:47	65.46	Rubin	z	18.52 ± 0.01
2026-05-26T23:28:32	66.46	Rubin	g	19.66 ± 0.01
2026-05-29T00:47:35	68.51	Rubin	g	19.63 ± 0.01
2026-05-29T00:51:43	68.51	Rubin	i	18.83 ± 0.01
2026-05-30T00:57:00	69.52	Rubin	z	18.65 ± 0.01
2026-05-30T23:25:19	70.45	Rubin	g	19.71 ± 0.01
2026-05-30T23:26:00	70.46	Rubin	g	19.71 ± 0.01
2026-06-04T00:51:41	74.51	Rubin	i	18.94 ± 0.01

Note. The photometry was queried through the Babamul alert broker (T. Jegou du Laz et al. 2026) using Object ID 314003014107006318. Times ΔT are given relative to the EP trigger. The photometry has not been corrected for Galactic reddening $E(B-V) = 0.02$ mag (E. F. Schlafly & D. P. Finkbeiner 2011).

(This table is available in its entirety in machine-readable form in the online article.)

Table 3
Log of Spectroscopic Observations of EP260321a/SN 2026gzf

Start Date (UTC)	δt (days)	Telescope	Instrument	Grating	Angle (deg)	Exposure (s)
2026-03-24 19:11:27	3.28	SALT	RSS	pg0700	4.6	2100
2026-03-25 03:35:06	3.63	HET	LRS2	LRS2-B	4.6	1800
2026-03-27 18:40:03	6.26	SALT	RSS	pg0700	4.6	2100
2026-04-01 19:02:08	11.27	SALT	RSS	pg0700	4.6	2100
2026-04-05 17:50:18	15.22	SALT	RSS	pg0700	4.6	2100
2026-04-08 04:33:00	17.67	Mayall	DESI	⋯	⋯	1200
2026-04-13 18:36:10	23.25	SALT	RSS	pg0700	4.6	2100
2026-04-23 03:38:37	32.63	Mayall	DESI	⋯	⋯	1200
2026-05-01 17:25:57	41.21	SALT	RSS	pg0700	7.6	2100
2026-05-09 17:00:30	49.19	SALT	RSS	pg0700	7.6	2100
2026-05-14 03:40:38	53.63	Mayall	DESI	⋯	⋯	1200
2026-05-14 17:17:51	54.20	SALT	RSS	pg0700	4.6	2100

Appendix B
Afterglow Constraints

In Figure 18, we show additional afterglow model constraints generated using `VegasAfterglow`; see Section 3.4 for further discussion.

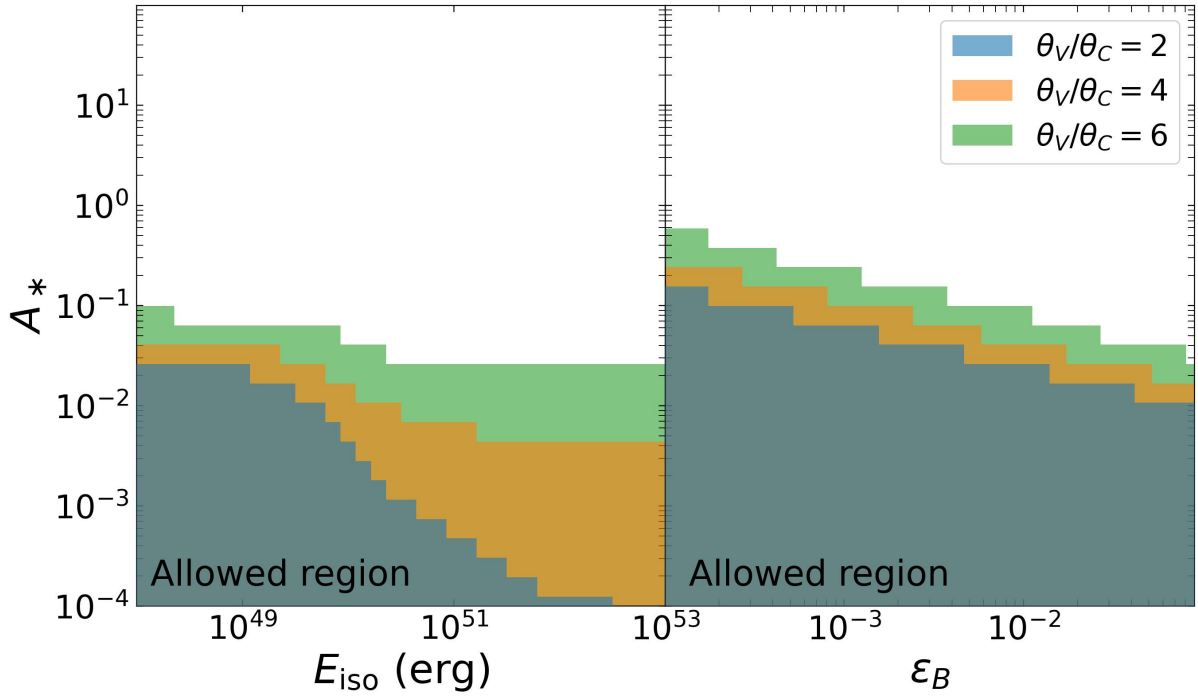

Figure 18. Allowed parameter space (shaded regions) for afterglow nondetection, assuming a Gaussian-structured jet, at 158 Mpc ($z = 0.0344$). Left: allowed values of the density A_* vs. the isotropic-equivalent kinetic energy at the jet's core $E_{\rm kin}$ for different viewing angles $\theta_{\rm v}/\theta_{\rm c}$. We have fixed $\theta_{\rm c} = 0.15$ rad, $\varepsilon_{\rm e} = 0.1$, $\varepsilon_{\rm B} = 0.01$, $p = 2.2$, and $\Gamma_0 = 100$. Right: similar to the left panel but instead as a function of $\varepsilon_{\rm B}$ for fixed $E_{\rm kin} = 10^{48}$ erg.

Appendix C
Archival DECam Time Series

We built an archival lightcurve of the source prior to its explosion using DECam data spanning 12.8–7.9 yr prior to explosion, see Figure 19. The source is visible in all previous images of this field (Figure 1), including in other surveys such as PS1[38] (e.g., AT 2018mtl; K. A. Sankar et al. 2026), SDSS, or DSS. This is potentially due to pre-explosion activity akin to that seen in luminous blue variables (LBVs; K. Weis & D. J. Bomans 2020; N. Smith 2026), as first suggested by N. R. Tanvir et al. (2026) and shown more clearly by T.-W. Chen et al. (2026) based on archival PS1 observations. We do not observe significant variability in the DECam data (which is consistent with T.-W. Chen et al. (2026), who also analyze these data; see their Figure 7). In the DECam data, the source is persistently blue in color ($g - i \approx -1.3$ mag). The absolute magnitude is $M_r \approx -15.7$ mag at a redshift of $z = 0.0344$. This brightness is at the very extreme end of previous LBV activity (e.g., N. Smith et al. 2010, 2011, 2014, 2020, 2022; C. S. Kochanek et al. 2011) and may suggest a dominant contribution from an existing H II region or compact dwarf galaxy, as suggested by T.-W. Chen et al. (2026), J. C. Rastinejad et al. (2026), A. Martin-Carrillo et al. (2026), W. Yuan et al. (2026), though with varying inferences on the stellar mass of the compact source ranging from 10^7 to $10^8\,M_\odot$. This is due to different choices regarding the aperture size across different surveys/filters. We note that given this source is visible in all images of this field, it is unclear what contribution is persistent versus transient behavior, as difference imaging can only be performed using the oldest images, which may still contain transient activity. Regardless, the PS1 variability observed by T.-W. Chen et al. (2026), which is at the level of $M_r \approx -14$ mag (see their Figure 3), points to an extreme behavior of the progenitor star leading up to terminal collapse. The exact nature of this pre-explosion source, and the contribution of the possible LBV brightness, will become clear as the SN fades away.

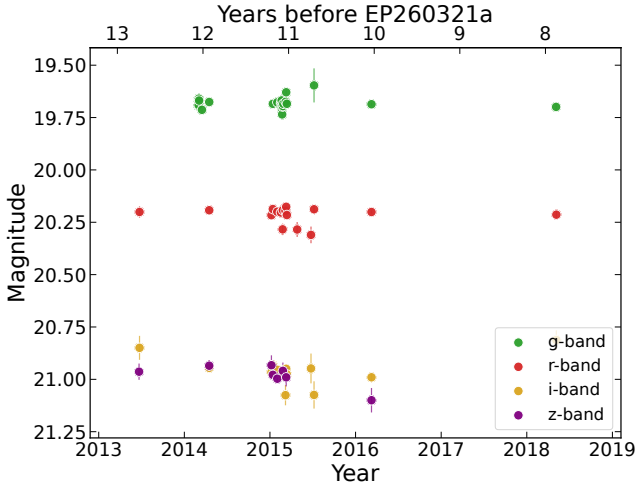

Figure 19. Archival DECam lightcurve of the pre-explosion source (Figure 1) at the location of EP260321a/SN 2026gzf in the *griz* bands.

[38] https://www.wis-tns.org/object/2018mtl

ORCID iDs

Brendan O'Connor https://orcid.org/0000-0002-9700-0036
Xander J. Hall https://orcid.org/0000-0002-9364-5419
Malte Busmann https://orcid.org/0009-0001-0574-2332
Daniel Gruen https://orcid.org/0000-0003-3270-7644
Alberto Floris https://orcid.org/0009-0004-1671-5454
Tomás Cabrera https://orcid.org/0000-0002-1270-7666
Ziyuan Zhu https://orcid.org/0009-0001-8023-5701
Antonella Palmese https://orcid.org/0000-0002-6011-0530
Dylan Green https://orcid.org/0000-0002-0676-3661
John Banovetz https://orcid.org/0000-0003-0776-8859
Julius Gassert https://orcid.org/0009-0008-2754-1946
Christopher L. Fryer https://orcid.org/0000-0003-2624-0056
Roberto Ricci https://orcid.org/0000-0003-4631-1528
Eleonora Troja https://orcid.org/0000-0002-1869-7817
Surya Shivaprasad https://orcid.org/0009-0006-1510-4648
Gregory R. Zeimann https://orcid.org/0000-0003-2307-0629
Ariel J. Amsellem https://orcid.org/0000-0003-3433-2698
Stephen Bailey https://orcid.org/0000-0003-4162-6619
Segev BenZvi https://orcid.org/0000-0001-5537-4710
Simone Dichiara https://orcid.org/0000-0001-6849-1270
Hendrik van Eerten https://orcid.org/0000-0002-8680-8718
Jeremy Hare https://orcid.org/0000-0002-8548-482X
Lei Hu https://orcid.org/0000-0001-7201-1938
Keerthi Kunnumkai https://orcid.org/0009-0000-4830-1484
Konstantin Malanchev https://orcid.org/0000-0001-7179-7406
Mitra Maleki https://orcid.org/0009-0001-5050-6232
Michael J. Moss https://orcid.org/0000-0002-1103-7082
Dheeraj Pasham https://orcid.org/0000-0003-1386-7861
Christoph Ries https://orcid.org/0009-0006-6697-8548
Geoffrey Ryan https://orcid.org/0000-0001-9068-7157
David Schlegel https://orcid.org/0000-0002-5042-5088
Michael Schmidt https://orcid.org/0009-0003-1323-9774
Yu-Han Yang https://orcid.org/0000-0003-0691-6688

References

Abazajian, K. N., Adelman-McCarthy, J. K., Agüeros, M. A., et al. 2009, ApJS, 182, 543
Afsariardchi, N., Drout, M. R., Khatami, D. K., et al. 2021, ApJ, 918, 89
Ahumada, T., Hall, X. J., Perley, D. A. & Zwicky Transient Facility 2026, GCN, 44084, 1
Allende Prieto, C., Lambert, D. L., & Asplund, M. 2001, ApJL, 556, L63
Alp, D., & Larsson, J. 2020, ApJ, 896, 39
Anand, S., Barnes, J., Yang, S., et al. 2024, ApJ, 962, 68
Andreoni, I., Coughlin, M. W., Perley, D. A., et al. 2022, Natur, 612, 430
Andrews, S., Fryer, C., Even, W., Jones, S., & Pignatari, M. 2020, ApJ, 890, 35
Arnaud, K. A. 1996, ASPC, 101, 17
Arnett, W. D. 1982, ApJ, 253, 785
Asplund, M., Grevesse, N., Sauval, A. J., Allende Prieto, C., & Kiselman, D. 2004, A&A, 417, 751
Asplund, M., Grevesse, N., Sauval, A. J., & Scott, P. 2009, ARA&A, 47, 481
Astropy Collaboration, Price-Whelan, A. M., Lim, P. L., et al. 2022, ApJ, 935, 167
Astropy Collaboration, Price-Whelan, A. M., Sipőcz, B. M., et al. 2018, AJ, 156, 123

Baldwin, J. A., Phillips, M. M., & Terlevich, R. 1981, PASP, 93, 5
Barthelmy, S. D., Barbier, L. M., Cummings, J. R., et al. 2005, SSRv, 120, 143
Bauer, F. E., Treister, E., Schawinski, K., et al. 2017, MNRAS, 467, 4841
Bayless, A. J., Even, W., Frey, L. H., et al. 2015, ApJ, 805, 98
Bayless, A. J., Fryer, C., Brown, P. J., et al. 2022, ApJ, 931, 15
Bellm, E. C., Kulkarni, S. R., Graham, M. J., et al. 2018, PASP, 131, 018002
Bertin, E. 2006, ASPC, 351, 112
Bertin, E. 2010, SWarp: Resampling and Co-adding FITS Images Together, ascl:1010.068
Bertin, E., & Arnouts, S. 1996, A&AS, 117, 393
Bertin, E., Mellier, Y., Radovich, M., et al. 2002, ASPC, 281, 228
Bradley, L., Sipőcz, B., Robitaille, T., et al. 2024, astropy/photutils: v2.0.2, Zenodo, doi:10.5281/zenodo.13989456
Briel, M. M., Fragos, T., Salafia, O. S., et al. 2025, A&A, 701, A84
Buckley, D. A. H., Swart, G. P., & Meiring, J. G. 2006, SPIE, 6267, 62670Z
Burrows, D. N., Hill, J. E., Nousek, J. A., et al. 2005, SSRv, 120, 165
Busmann, M., O'Connor, B., Sommer, J., et al. 2025, A&A, 701, A225
Cabrera, T., Palmese, A., Hu, L., et al. 2024, PhRvD, 110, 123029
Campana, S., Mangano, V., Blustin, A. J., et al. 2006a, Natur, 442, 1008
Campana, S., Tagliaferri, G., Lazzati, D., et al. 2006b, A&A, 454, 113
Cano, Z. 2013, MNRAS, 434, 1098
Cano, Z., Bersier, D., Guidorzi, C., et al. 2011, ApJ, 740, 41
Cano, Z., de Ugarte Postigo, A., Pozanenko, A., et al. 2014, A&A, 568, A19
Cano, Z., Izzo, L., de Ugarte Postigo, A., et al. 2017b, A&A, 605, A107
Cano, Z., Wang, S.-Q., Dai, Z.-G., & Wu, X.-F. 2017a, AdAst, 2017, 8929054
CASA Team, Bean, B., Bhatnagar, S., et al. 2022, PASP, 134, 114501
Chabrier, G. 2003, PASP, 115, 763
Chambers, K. C., Magnier, E. A., Metcalfe, N., et al. 2016, arXiv:1612.05560
Chandra, P., & Frail, D. A. 2012, ApJ, 746, 156
Chen, T.-W., Aryan, A., Yang, S., et al. 2026, arXiv:2606.10009
Chevalier, R. A., & Fransson, C. 2008, ApJL, 683, L135
Chonis, T. S., Hill, G. J., Lee, H., Tuttle, S. E., & Vattiat, B. L. 2014, SPIE, 9147, 91470A
Chonis, T. S., Hill, G. J., Lee, H., et al. 2016, SPIE, 9908, 99084C
Chornock, R., Berger, E., Levesque, E. M., et al. 2010, arXiv:1004.2262
Christensen, L., Vreeswijk, P. M., Sollerman, J., et al. 2008, A&A, 490, 45
Clocchiatti, A., Wheeler, J. C., Brotherton, M. S., et al. 1996, ApJ, 462, 462
Colgate, S. A. 1974, ApJ, 187, 333
Colosimo, J. M., Fox, D. B., Falcone, A. D., et al. 2024, ApJ, 969, 138
Coppejans, D. L., Margutti, R., Terreran, G., et al. 2020, ApJL, 895, L23
Corcoran, G., Martin-Carrillo, A., Izzo, L., et al. 2026, GCN, 44105, 1
Corsi, A., Ho, A. Y. Q., Cenko, S. B., et al. 2023, ApJ, 953, 179
Cotter, L., Martin-Carrillo, A., Eyles-Ferris, R. A. J., et al. 2026, arXiv:2606.06213
Crosato Menegazzi, L., Fujibayashi, S., Takahashi, K., & Ishii, A. 2024, MNRAS, 529, 178
Dean, C., & Fernández, R. 2024, PhRvD, 109, 083010
D'Elia, V., Campana, S., D'Aì, A., et al. 2018, A&A, 619, A66
D'Elia, V., Pian, E., Melandri, A., et al. 2015, A&A, 577, A116
DESI Collaboration, Abdul-Karim, M., Adame, A. G., et al. 2025a, AJ, 171, 285
DESI Collaboration, Abdul Karim, M., Adame, A. G., et al. 2026, AJ, 171, 285
DESI Collaboration, Abdul-Karim, M., Aguilar, J., et al. 2025b, PhRvD, 112, 083515
DESI Collaboration, Adame, A. G., Aguilar, J., et al. 2024, AJ, 168, 58
DESI Collaboration, Aghamousa, A., Aguilar, J., et al. 2016, arXiv:1611.00037
Dessart, L., Hillier, D. J., Li, C., & Woosley, S. 2012, MNRAS, 424, 2139
de Ugarte Postigo, A., García García, L., Becerra, R. L., et al. 2026, GCN, 44091, 1
Disberg, P., Lankreijer, A., Chruślińska, M., et al. 2025, A&A, 703, A288
Evans, P. A., Beardmore, A. P., Page, K. L., et al. 2007, A&A, 469, 379
Evans, P. A., Beardmore, A. P., Page, K. L., et al. 2009, MNRAS, 397, 1177
Eyles-Ferris, R. A. J., Jonker, P. G., Levan, A. J., et al. 2025, ApJL, 988, L14
Falcone, A. D., Colosimo, J. M., Wages, M., et al. 2024, SPIE, 13093, 1309317
Falk, S. W. 1978, ApJL, 225, L133
Faran, T., & Sari, R. 2019, ApJ, 884, 41
Ferrero, P., Kann, D. A., Zeh, A., et al. 2006, A&A, 457, 857
Filippenko, A. V. 1997, ARA&A, 35, 309
Finneran, G., Cotter, L., & Martin-Carrillo, A. 2025a, A&A, 700, A200
Finneran, G., Cotter, L., & Martin-Carrillo, A. 2025b, A&C, 52, 100954
Foreman-Mackey, D., Hogg, D. W., Lang, D., & Goodman, J. 2013, PASP, 125, 306
Fruscione, A., McDowell, J. C., Allen, G. E., et al. 2006, SPIE, 6270, 62701V
Fryer, C. L., Burns, E., Colosimo, J. M., Negro, M., & O'Connor, B. 2026, arXiv:2603.00820
Fryer, C. L., Burns, E., Ho, A. Y. Q., et al. 2025, ApJ, 986, 185
Fryer, C. L., Fontes, C. J., Warsa, J. S., et al. 2020, ApJ, 898, 123
Gaia Collaboration 2020, yCat, I/350,
Gaia Collaboration, Brown, A. G. A., Vallenari, A., et al. 2021, A&A, 649, A1
Galama, T. J., Vreeswijk, P. M., van Paradijs, J., et al. 1998, Natur, 395, 670
Ganss, R., Pledger, J. L., Sansom, A. E., et al. 2022, MNRAS, 512, 1541
Ganss, R., Pledger, J. L., Sansom, A. E., et al. 2025, MNRAS, 543, 2374
Gehrels, N., Chincarini, G., Giommi, P., et al. 2004, ApJ, 611, 1005
Gezari, S., Dessart, L., Basa, S., et al. 2008, ApJL, 683, L131
Ghisellini, G., Ghirlanda, G., Mereghetti, S., et al. 2006, MNRAS, 372, 1699
Glennie, A., Jonker, P. G., Fender, R. P., Nagayama, T., & Pretorius, M. L. 2015, MNRAS, 450, 3765
Goldberg, J. A., Jiang, Y.-F., Bildsten, L., et al. 2022, ApJ, 933, 164
Gössl, C. A., & Riffeser, A. 2002, A&A, 381, 1095
Graham, M. J., Kulkarni, S. R., Bellm, E. C., et al. 2019, PASP, 131, 078001
Granot, J., & Sari, R. 2002, ApJ, 568, 820
Guy, J., Bailey, S., Kremin, A., et al. 2023, AJ, 165, 144
Hall, X. J., Banovez, J., Palmese, A., et al. 2026a, TNSAN, 81, 1
Hall, X. J., Palmese, A., BenZvi, S., et al. 2026b, The DESI Transients Survey: Legacy Classifications and Methodology, v3, Zenodo, doi:10.5281/zenodo.19653826
Hall, X. J., Palmese, A., BenZvi, S., et al. 2026c, arXiv:2601.12611
Hall, X. J., Palmese, A., O'Connor, B., et al. 2026d, ApJL, 1001, L20
Hamidani, H., Sato, Y., Kashiyama, K., et al. 2025, ApJL, 986, L4
Han, X. H., Hammer, F., Liang, Y. C., et al. 2010, A&A, 514, A24
Hill, G. J., Lee, H., MacQueen, P. J., et al. 2021, AJ, 162, 298
Hjorth, J., & Bloom, J. S. 2012, in Gamma-Ray Bursts, ed. C. Kouveliotou, R.A.M.J Wijers, & S. Woosely (Cambridge Univ. Press), 169
Ho, A. Y. Q., Perley, D. A., Kulkarni, S. R., et al. 2020, ApJ, 895, 49
Ho, A. Y. Q., Phinney, E. S., Ravi, V., et al. 2019, ApJ, 871, 73
Hopp, U., Bender, R., Grupp, F., et al. 2014, SPIE, 9145, 91452D
Hu, L., Cabrera, T., Palmese, A., et al. 2025, ApJL, 990, L46
Hu, L., Cabrera, T., Palmese, A., et al. 2026, arXiv:2603.08593
Hu, L., Wang, L., Chen, X., & Yang, J. 2022, ApJ, 936, 157
Huang, Q. J., Zou, Z.-C., Li, D. Y., et al. 2026, GCN, 44075, 1
Irwin, C. M., & Chevalier, R. A. 2016, MNRAS, 460, 1680
Irwin, C. M., & Hotokezaka, K. 2025a, MNRAS, 541, L85
Irwin, C. M., & Hotokezaka, K. 2025b, MNRAS, 542, 1269
Irwin, C. M., & Hotokezaka, K. 2025c, MNRAS, 543, 2917
Irwin, C. M., Linial, I., Nakar, E., Piran, T., & Sari, R. 2021, MNRAS, 508, 5766
Ivezić, Ž., Kahn, S. M., Tyson, J. A., et al. 2019, ApJ, 873, 111
Izzo, L., de Ugarte Postigo, A., Maeda, K., et al. 2019, Natur, 565, 324
Izzo, L., Thöne, C. C., Schulze, S., et al. 2017, MNRAS, 472, 4480
Japelj, J., Vergani, S. D., Salvaterra, R., et al. 2018, A&A, 617, A105
Jegou du Laz, T., Coughlin, M. W., Bachant, P., et al. 2026, PASP, 138, 064503
Jonker, P. G., Glennie, A., Heida, M., et al. 2013, ApJ, 779, 14
Kasen, D. 2010, ApJ, 708, 1025
Kashyap, V. L., van Dyk, D. A., Connors, A., et al. 2010, ApJ, 719, 900
Katz, B., Sapir, N., & Waxman, E. 2012a, IAUS, 279, 274
Katz, B., Sapir, N., & Waxman, E. 2012b, ApJ, 747, 147
Kauffmann, G., Heckman, T. M., Tremonti, C., et al. 2003, MNRAS, 346, 1055
Kennicutt, R. C. J. 1998, ARA&A, 36, 189
Kewley, L. J., Dopita, M. A., Sutherland, R. S., Heisler, C. A., & Trevena, J. 2001, ApJ, 556, 121
Kewley, L. J., Groves, B., Kauffmann, G., & Heckman, T. 2006, MNRAS, 372, 961
Klein, R. I., & Chevalier, R. A. 1978, ApJL, 223, L109
Kochanek, C. S., Szczygiel, D. M., & Stanek, K. Z. 2011, ApJ, 737, 76
Kouveliotou, C., Woosley, S. E., Patel, S. K., et al. 2004, ApJ, 608, 872
Krühler, T., Kuncarayakti, H., Schady, P., et al. 2017, A&A, 602, A85
Krühler, T., Malesani, D., Fynbo, J. P. U., et al. 2015, A&A, 581, A125
Kulkarni, S. R., Harrison, F. A., Grefenstette, B. W., et al. 2021, arXiv:2111.15608
Lang-Bardl, F., Bender, R., Goessl, C., et al. 2016, SPIE, 9908, 990844
Laskar, T., Escorial, A. R., Schroeder, G., et al. 2022, ApJL, 935, L11
Lawrence, A., Warren, S. J., Almaini, O., et al. 2007, MNRAS, 379, 1599
Lee, M.-H., Aryan, A., Chen, T.-W., et al. 2026, GCN, 44070, 1
Leung, J. K., Izzo, L., de Colle, F., & Drout, M. R. 2026, GCN, 44229, 1
Levesque, E. M., Berger, E., Kewley, L. J., & Bagley, M. M. 2010a, AJ, 139, 694

Levesque, E. M., Berger, E., Soderberg, A. M., & Chornock, R. 2011, ApJ, 739, 23
Levesque, E. M., Chornock, R., Soderberg, A. M., Berger, E., & Lunnan, R. 2012, ApJ, 758, 92
Levesque, E. M., Kewley, L. J., Berger, E., & Zahid, H. J. 2010b, AJ, 140, 1557
Levinson, A., & Nakar, E. 2020, PhR, 866, 1
Li, L.-X. 2007, MNRAS, 375, 240
Li, W. X., Zhu, Z. P., Zou, X. Z., et al. 2025, arXiv:2504.17034
Liang, R.-D., Li, W.-X., Liu, L.-D., et al. 2026, ApJ, 999, 239
Lien, A., Sakamoto, T., Gehrels, N., et al. 2014, ApJ, 783, 24
Lindegren, L., Klioner, S. A., Hernández, J., et al. 2021, A&A, 649, A2
Liu, X., Xu, D., Tinyanont, S., et al. 2026, GCN, 44087, 1
Lovegrove, E., Woosley, S. E., & Zhang, W. 2017, ApJ, 845, 103
MacFadyen, A. I., & Woosley, S. E. 1999, ApJ, 524, 262
Maeda, K., Nomoto, K., Mazzali, P. A., & Deng, J. 2006, ApJ, 640, 854
Malesani, D., Fynbo, J. P. U., Hjorth, J., et al. 2009, ApJL, 692, L84
Margutti, R., Alexander, K. D., Xie, X., et al. 2018, ApJL, 856, L18
Margutti, R., Berger, E., Fong, W., et al. 2017, ApJL, 848, L20
Margutti, R., Metzger, B. D., Chornock, R., et al. 2019, ApJ, 872, 18
Margutti, R., Soderberg, A. M., Wieringa, M. H., et al. 2013a, ApJ, 778, 18
Margutti, R., Zaninoni, E., Bernardini, M. G., et al. 2013b, MNRAS, 428, 729
Marino, R. A., Rosales-Ortega, F. F., Sánchez, S. F., et al. 2013, A&A, 559, A114
Martin-Carrillo, A., Thöne, C. C., Leung, J. K., et al. 2026, arXiv:2606.10002
Masci, F. J., Laher, R. R., Rusholme, B., et al. 2018, PASP, 131, 018003
Mazzali, P. A., Deng, J., Nomoto, K., et al. 2006, Natur, 442, 1018
Mazzali, P. A., Nomoto, K., Patat, F., & Maeda, K. 2001, ApJ, 559, 1047
Mazzali, P. A., Pian, E., Bufano, F., & Ashall, C. 2021, MNRAS, 505, 4106
Mazzali, P. A., Valenti, S., Della Valle, M., et al. 2008, Sci, 321, 1185
Melandri, A., Malesani, D. B., Izzo, L., et al. 2019, MNRAS, 490, 5366
Meza, N., & Anderson, J. P. 2020, A&A, 641, A177
MichałowskI, M. J., Xu, D., Stevens, J., et al. 2018, A&A, 616, A169
Miller, T. N., Doel, P., Gutierrez, G., et al. 2024, AJ, 168, 95
Modjaz, M., Bianco, F. B., Siwek, M., et al. 2020, ApJ, 892, 153
Modjaz, M., Kewley, L., Bloom, J. S., et al. 2011, ApJL, 731, L4
Modjaz, M., Li, W., Butler, N., et al. 2009, ApJ, 702, 226
Modjaz, M., Liu, Y. Q., Bianco, F. B., & Graur, O. 2016, ApJ, 832, 108
Moss, M. J., Lien, A. Y., Cenko, S. B., Guiriec, S., & Markwardt, C. B. 2026, ApJ, 1002, 27
Moss, M. J., Lien, A. Y., Guiriec, S., Cenko, S. B., & Sakamoto, T. 2022, ApJ, 927, 157
Myers, A. D., Moustakas, J., Bailey, S., et al. 2023, AJ, 165, 50
Nakar, E. 2015, ApJ, 807, 172
Nakar, E., & Sari, R. 2010, ApJ, 725, 904
Nakar, E., & Sari, R. 2012, ApJ, 747, 88
NASA High Energy Astrophysics Science Archive Research Center (HEASARC) 2014, HEAsoft: Unified Release of FTOOLS and XANADU, ascl:1408.004
Niblett, A. E., Fryer, D. A., & Fryer, C. L. 2025, ApJ, 994, 259
O'Connor, B., Beniamini, P., Troja, E., et al. 2025a, ApJL, 993, L37
O'Connor, B., Pasham, D., Andreoni, I., et al. 2025b, ApJL, 979, L30
O'Connor, B., Ricci, R., Troja, E., et al. 2025c, ApJL, 995, L47
O'Dwyer, T., Corsi, A., Yang, S., et al. 2026, ApJ, 1002, 194
Perley, D. A., Ho, A. Y. Q., Fausnaugh, M., et al. 2025, MNRAS, 537, 1
Pettini, M., & Pagel, B. E. J. 2004, MNRAS, 348, L59
Pian, E., Amati, L., Antonelli, L. A., et al. 1999, A&AS, 138, 463
Pian, E., Amati, L., Antonelli, L. A., et al. 2000, ApJ, 536, 778
Pian, E., Giommi, P., Amati, L., et al. 2004, AdSpR, 34, 2711
Pian, E., Mazzali, P. A., Masetti, N., et al. 2006, Natur, 442, 1011
Piro, A. L., Chang, P., & Weinberg, N. N. 2010, ApJ, 708, 598
Planck Collaboration, Aghanim, N., Akrami, Y., et al. 2020, A&A, 641, A6
Poppett, C., Tyas, L., Aguilar, J., et al. 2024, AJ, 168, 245
Prentice, S. J., Ashall, C., James, P. A., et al. 2019, MNRAS, 485, 1559
Prentice, S. J., & Mazzali, P. A. 2017, MNRAS, 469, 2672
Prentice, S. J., Mazzali, P. A., Pian, E., et al. 2016, MNRAS, 458, 2973
Quirola-Vásquez, J., Bauer, F. E., Jonker, P. G., et al. 2022, A&A, 663, A168
Quirola-Vásquez, J., Bauer, F. E., Jonker, P. G., et al. 2023, A&A, 675, A44
Ramsey, L. W., Adams, M. T., Barnes, T. G., et al. 1998, SPIE, 3352, 34
Rastinejad, J., Srinivasaragavan, G., & Ahumada, T. 2026, GCN, 44107, 1
Rastinejad, J. C., Levan, A. J., Jonker, P. G., et al. 2025, ApJL, 988, L13
Rastinejad, J. C., Srinivasaragavan, G., Sarin, N., et al. 2026, arXiv:2606.10011
Rhoads, J. E. 2003, ApJ, 591, 1097
Ricci, R., Troja, E., Yang, Y.-H., et al. 2025, ApJL, 979, L28
Rodríguez, Ó., Maoz, D., & Nakar, E. 2023, ApJ, 955, 71
Russell, S. C., & Dopita, M. A. 1990, ApJS, 74, 93
Sagiv, I., Gal-Yam, A., Ofek, E. O., et al. 2014, AJ, 147, 79
Sankar, K. A., Aryan, A., Chen, T.-W., et al. 2026, GCN, 44089, 1
Sapir, N., Katz, B., & Waxman, E. 2011, ApJ, 742, 36
Sari, R., Piran, T., & Narayan, R. 1998, ApJL, 497, L17
Schady, P., Krühler, T., Greiner, J., et al. 2015, A&A, 579, A126
Schawinski, K., Justham, S., Wolf, C., et al. 2008, Sci, 321, 223
Schlafly, E. F., & Finkbeiner, D. P. 2011, ApJ, 737, 103
Schlafly, E. F., Kirkby, D., Schlegel, D. J., et al. 2023, AJ, 166, 259
Schroeder, G., Ho, A. Y. Q., Dastidar, R. G., et al. 2025, ApJ, 995, 61
Shetrone, M., Cornell, M. E., Fowler, J. R., et al. 2007, PASP, 119, 556
Shvartzvald, Y., Waxman, E., Gal-Yam, A., et al. 2024, ApJ, 964, 74
Sironi, L., Keshet, U., & Lemoine, M. 2015, SSRv, 191, 519
Skrutskie, M. F., Cutri, R. M., Stiening, R., et al. 2006, AJ, 131, 1163
Smith, N. 2017, in Handbook of Supernovae, ed. A. W. Alsabti & P. Murdin (Springer), 403
Smith, N. 2026, Encyclopedia of Astrophysics, Vol. 2 (Elsevier), 508
Smith, N., Andrews, J. E., Filippenko, A. V., et al. 2022, MNRAS, 515, 71
Smith, N., E Andrews, J., Moe, M., et al. 2020, MNRAS, 492, 5897
Smith, N., Li, W., Silverman, J. M., Ganeshalingam, M., & Filippenko, A. V. 2011, MNRAS, 415, 773
Smith, N., Mauerhan, J. C., & Prieto, J. L. 2014, MNRAS, 438, 1191
Smith, N., Miller, A., Li, W., et al. 2010, AJ, 139, 1451
Soderberg, A. M., Berger, E., Page, K. L., et al. 2008, Natur, 453, 469
Soderberg, A. M., Kulkarni, S. R., Nakar, E., et al. 2006, Natur, 442, 1014
Sollerman, J., Jaunsen, A. O., Fynbo, J. P. U., et al. 2006, A&A, 454, 503
Srinivasaragavan, G. P., Hamidani, H., Schroeder, G., et al. 2025a, ApJL, 988, L60
Srinivasaragavan, G. P., Li, D., Hall, X. J., et al. 2025b, arXiv:2512.10239
Srinivasaragavan, G. P., Yang, S., Anand, S., et al. 2024, ApJ, 976, 71
Starling, R. L. C., Wiersema, K., Levan, A. J., et al. 2011, MNRAS, 411, 2792
Sun, H., Li, W. X., Liu, L. D., et al. 2025, NatAs, 9, 1073
Sun, H., Liu, H.-Y., Pan, H.-W., et al. 2022, ApJ, 927, 224
Svirski, G., & Nakar, E. 2014a, ApJ, 788, 113
Svirski, G., & Nakar, E. 2014b, ApJL, 788, L14
Taddia, F., Sollerman, J., Fremling, C., et al. 2019, A&A, 621, A71
Taddia, F., Stritzinger, M. D., Bersten, M., et al. 2018, A&A, 609, A136
Tanga, M., Krühler, T., Schady, P., et al. 2018, A&A, 615, A136
Tanvir, N. R., Izzo, L., Levan, A. J., et al. 2026, GCN, 44082, 1
Thöne, C. C., Christensen, L., Prochaska, J. X., et al. 2014, MNRAS, 441, 2034
Thöne, C. C., de Ugarte Postigo, A., Izzo, L., et al. 2024, A&A, 690, A66
Thöne, C. C., Izzo, L., Flores, H., et al. 2021, A&A, 656, A136
Thöne, C. C., Michałowski, M. J., Leloudas, G., et al. 2009, ApJ, 698, 1307
Tiengo, A., Mereghetti, S., Ghisellini, G., Tavecchio, F., & Ghirlanda, G. 2004, A&A, 423, 861
Toy, V. L., Cenko, S. B., Silverman, J. M., et al. 2016, ApJ, 818, 79
Troja, E., Piro, L., van Eerten, H., et al. 2017, Natur, 551, 71
Volnova, A. A., Pruzhinskaya, M. V., Pozanenko, A. S., et al. 2017, MNRAS, 467, 3500
Wang, J., Zhu, Z. P., Xu, D., et al. 2018, ApJ, 867, 147
Wang, X.-Y., Li, Z., Waxman, E., & Mészáros, P. 2007, ApJ, 664, 1026
Wang, Y., Chen, C., & Zhang, B. 2026, JHEAp, 50, 100490
Watson, D., Hjorth, J., Levan, A., et al. 2004, ApJL, 605, L101
Waxman, E., & Katz, B. 2017, in Handbook of Supernovae, ed. A. W. Alsabti & P. Murdin (Springer), 967
Waxman, E., Mészáros, P., & Campana, S. 2007, ApJ, 667, 351
Weaver, T. A. 1976, ApJS, 32, 233
Weis, K., & Bomans, D. J. 2020, Galax, 8, 20
Willingale, R., Starling, R. L. C., Beardmore, A. P., Tanvir, N. R., & O'Brien, P. T. 2013, MNRAS, 431, 394
Wolf, C., & Podsiadlowski, P. 2007, MNRAS, 375, 1049
Woosley, S. E. 1993, ApJ, 405, 273
Woosley, S. E., & Bloom, J. S. 2006, ARA&A, 44, 507
Xu, D., Corcoran, G., An, J., et al. 2026, GCN, 44092, 1
Yang, S., & Sollerman, J. 2023, ApJS, 269, 40
Yaron, O., & Gal-Yam, A. 2012, PASP, 124, 668
Yuan, W., Dai, L., Feng, H., et al. 2025, SCPMA, 68, 239501
Yuan, W., Huang, Q.-J., Zhu, J.-P., et al. 2026, arXiv:2606.10014
Yuan, W., Zhang, C., Chen, Y., & Ling, Z. 2022, Handbook of X-ray and Gamma-ray Astrophysics, Vol. 86 (Springer)
Yuan, W., Zhang, C., Feng, H., et al. 2015, arXiv:1506.07735
Zauderer, B. A., Berger, E., Soderberg, A. M., et al. 2011, Natur, 476, 425
Zenati, Y., Siegel, D. M., Metzger, B. D., & Perets, H. B. 2020, MNRAS, 499, 4097